

# Diffusion Models Are Promising for *Ab Initio* Structure Solutions from Nanocrystalline Powder Diffraction Data

Gabe Guo<sup>1\*</sup>, Tristan Luca Saidi<sup>1</sup>, Maxwell W. Terban<sup>2</sup>, Simon J. L. Billinge<sup>3\*</sup>, and Hod Lipson<sup>4\*</sup>

<sup>1</sup>Columbia University, Department of Computer Science, New York, NY, USA, 10027

<sup>2</sup>Momentum Transfer, 68169 Mannheim, Germany

<sup>3</sup>Columbia University, Department of Applied Physics and Applied Mathematics, New York, NY, USA, 10027

<sup>4</sup>Columbia University, Department of Mechanical Engineering, New York, NY, USA, 10027

\*Correspondence: {gzg2104, sb2896, hod.lipson}@columbia.edu

## ABSTRACT

A major challenge in materials science is the determination of the structure of nanometer sized objects. Here we present a novel approach that uses a generative machine learning model based on a Diffusion model that is trained on 45,229 known structures. The model factors both the measured diffraction pattern as well as relevant statistical priors on the unit cell of atomic cluster structures. Conditioned only on the chemical formula and the information-scarce finite-size broadened powder diffraction pattern, we find that our model, PXRDNET, can successfully solve simulated nanocrystals as small as 10 Å across 200 materials of varying symmetry and complexity, including structures from all seven crystal systems. We show that our model can determine structural solutions with up to 81.5% accuracy, as measured by structural correlation. Furthermore, PXRDNET is capable of solving structures from noisy diffraction patterns gathered in real-world experiments. We suggest that data driven approaches, bootstrapped from theoretical simulation, will ultimately provide a path towards determining the structure of previously unsolved nano-materials.

## Introduction

The ongoing materials revolution of the past hundred years has been built upon the scientific community’s heightened understanding of atomic arrangements (*i.e.*, material structure) and the inherent dependence of material properties on this underlying structure. In regards to determining material structure, the *conditio sine qua non* is single crystal structure solution. In this optimal setting, despite the loss of phase information, the diffraction patterns contain maximal information content for the structure solution<sup>1</sup> and are often successful. Yet, in increasingly many practical settings, it is not feasible to obtain a pure single-crystal sample. This is especially acute for nanometer-sized atomic clusters, the so-called nanostructure problem<sup>2</sup>. In these cases the diffraction patterns have significant degradation in information content. Peak intensities must be extracted from overlapped peaks in powder diffraction patterns<sup>3</sup> and this problem is greatly amplified in nano-materials, defined as crystallites with dimensions below 1000 Å<sup>2</sup>, because the Bragg peaks become significantly broadened due to finite size effects. Our goal is to see whether the use of prior knowledge in the form of previously solved structures, used to train a generative AI model, can overcome this challenge of structure solution from information-degraded diffraction patterns.

In practice, for sufficiently simple structures it is possible to solve a structure from powder diffraction data alone<sup>3,4</sup>. In the case of nano-materials it is rarely possible to solve the structure *ab initio*<sup>5,6</sup>.

We use as input a powder x-ray diffraction (PXRD) pattern, measured over a limited range of momentum transfer,  $Q$ , with peak broadening due to crystallite nano-sizing. We note that, once demonstrated, the approach, can also be applied to powder patterns that have no finite-size broadening, resulting in a broadly applicable method for structure solution from powder and nano-powder diffraction data. The method shows great promise despite the highly degraded information content in the input patterns.

Although there are a number of works applying ML to problems in structure solution, we are not aware of any similar to our approach in method or breadth of applicability.<sup>7,8</sup> Much of the early work in this area used machine learning to predict isolated properties such as unit cell parameters, magnetism, phase composition and symmetry group of structures given PXRD patterns<sup>9-21</sup>. We also note that our problem is distinct from that of structure prediction, where generative artificial intelligence (AI) techniques have been used successfully to generate novel (never seen before) material structures that are presumably energetically stable<sup>22-25</sup>, *e.g.*, GNoME<sup>26</sup>, UniMat<sup>27</sup>, CDVAE<sup>28</sup>, MatterGen<sup>29</sup>.

Data Source	PDF Correlation ( $\uparrow$ )	Match Rate ( $\uparrow$ )	$R_{wp}^2$ ( $\downarrow$ )	Number Materials
PXRDNET				
MP-20 (10 Å)	0.798 $\pm$ 0.11	0.500	0.377 $\pm$ 0.26	200
MP-20 (100 Å)	0.791 $\pm$ 0.12	0.455	0.364 $\pm$ 0.27	200
Experimental	0.815 $\pm$ 0.09	0.400	0.460 $\pm$ 0.39	15
<i>Baseline: Latent Space Search</i>				
MP-20 (10 Å)	0.696 $\pm$ 0.10	0.180	0.643 $\pm$ 0.30	200
MP-20 (100 Å)	0.701 $\pm$ 0.10	0.205	0.635 $\pm$ 0.30	200
Experimental	0.693 $\pm$ 0.10	0.133	0.694 $\pm$ 0.26	15
<i>Baseline: Semi-Random</i>				
MP-20 (10 Å)	0.567 $\pm$ 0.15	0.005	0.986 $\pm$ 0.37	200
MP-20 (100 Å)	0.570 $\pm$ 0.15	0.010	0.989 $\pm$ 0.38	200
Experimental	0.580 $\pm$ 0.16	0.067	1.100 $\pm$ 0.37	15

**Table 1. Material Reconstruction Success Metrics:** *Data Source* refers to the source of the data, where "MP-20 ( $\{10, 100\}$  Å)" refers to PXRD patterns of simulated  $\{10, 100\}$  Å-scale nanomaterials from the MP-20-PXRD dataset<sup>28,36</sup>, and "Experimental" refers to PXRD patterns from real-world experimental data. "Baseline (MP-20, Experimental)" refers to results from semi-random search baselines on MP-20 and the Experimental dataset, respectively. *PDF Correlation* refers to the Pearson correlation coefficient<sup>37</sup> between the simulated pair distribution functions of the true material and of the predicted material; it ranges from  $0 \rightarrow 1$ , where higher is better; we calculate the mean and standard deviation over the testing set. *Match Rate* refers to the proportion of predicted structures that PyMatGen’s default material matching function<sup>38</sup> deemed to be a match with the ground truth; it ranges from  $0 \rightarrow 1$ , where higher is better.  $R_{wp}^2$  (otherwise known as the *R-Factor*) refers to the relative error between the PXRD pattern of the ground truth material and the PXRD pattern of the predicted material, where lower values are better<sup>4</sup>; we calculate the mean and standard deviation over the testing set.

ML has also been used to help with sub-tasks in the overall structure solution problem, such as structure solution for a limited number of crystal systems (*CrystalNet*<sup>30</sup>) and close-packed structures (*DeepStruc*<sup>31</sup>), AI accelerated mining of existing structural databases (*MLstructureMining*<sup>32</sup>), or single-crystal structural solutions (*Crysformer*<sup>33,34</sup>).

We find that our use of diffusion models for a fully end-to-end structure solution tool is highly promising. It was able to find plausible structures from information degraded PXRD patterns across broad classes of materials from all seven crystal systems. It was designed to output the lattice parameters and fractional atomic coordinates of atom in a unit cell of the structure, in a crystallographic setting that can be ingested by other programs that take crystal structures as inputs.

Owing to the inherent uncertainty when presented with information-scarce diffraction patterns, PXRDNET, via its Langevin dynamics-inspired conditional generative process<sup>35</sup>, generates multiple candidate structures that adhere to the input information. These candidates can be refined to search for global minimum structure solutions. It successfully found structure solutions for simulated nanocrystals as small as 10 Å, is successful across all seven crystal systems, and was shown to work on real-world experimentally gathered PXRD patterns.

To further community research efforts in structure solution, we also propose MP-20-PXRD, a benchmark task of inorganic materials and their corresponding simulated PXRD patterns. The data itself is curated from the Materials Project<sup>28,36</sup>, and our hope is that it provides a uniform standard of comparison for future computational materials scientists working on structure solutions from PXRD. Its advantages (aside from the PXRD information) are that the materials in the dataset are generally stable, experimentally synthesizable, and diverse, while containing at most 20 atoms in the unit cell<sup>28</sup>. It is freely downloadable at this link: [https://github.com/gabeguocdvae\\_xrd/tree/main/data/mp\\_20](https://github.com/gabeguocdvae_xrd/tree/main/data/mp_20).

## Results

### Nanostructure Evaluation Setup

Typically, a nanostructure is defined as that with crystalline size below 1000 Å<sup>39</sup>. To test the efficacy of our approach, we go two orders of magnitude below that and simulate PXRD patterns from crystalline sizes 10 Å and 100 Å with a mathematically principled filtering approach based on Fourier analysis<sup>40</sup> (described in Methods). As expected, the 10 Å case has more peak broadening (and therefore, information degradation)<sup>2,3</sup> than the 100 Å case. Visualizations of representative PXRD patterns are shown in Figure 1.

To our model, we input this nanoscale PXRD pattern and the chemical formula of materials from MP-20 (a subset of the Materials Project database)<sup>28,36</sup>. The model outputs a set of material structure predictions in the form of lattice parameters and

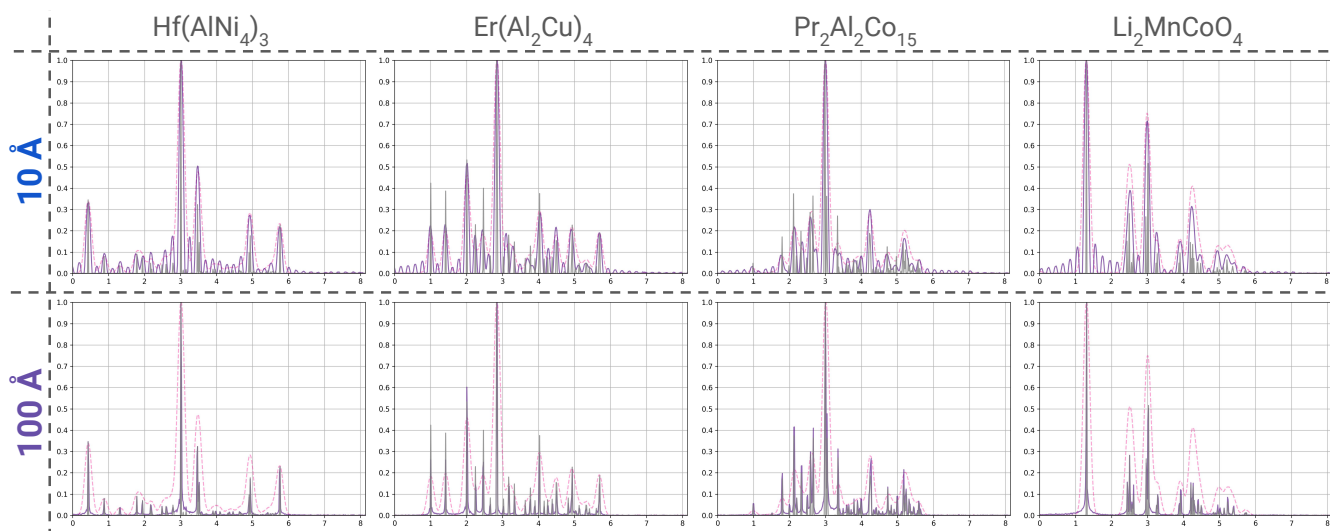


**Figure 1. Nanomaterial PXRD Patterns:** We simulate nanoscale shrinkage via the sinc filter, thereby broadening the PXRD peaks (purple lines) from the ideal pattern (gray lines). To improve model performance, we create a smoother target PXRD pattern (dotted pink lines) that removes the sharp ripples at the expense of further broadening the diffraction pattern. This is done via an additional Gaussian filter after the sinc filter. The horizontal axis is  $Q$  ( $\text{\AA}^{-1}$ ), and the vertical axis is scaled intensity (where 1 is maximal).

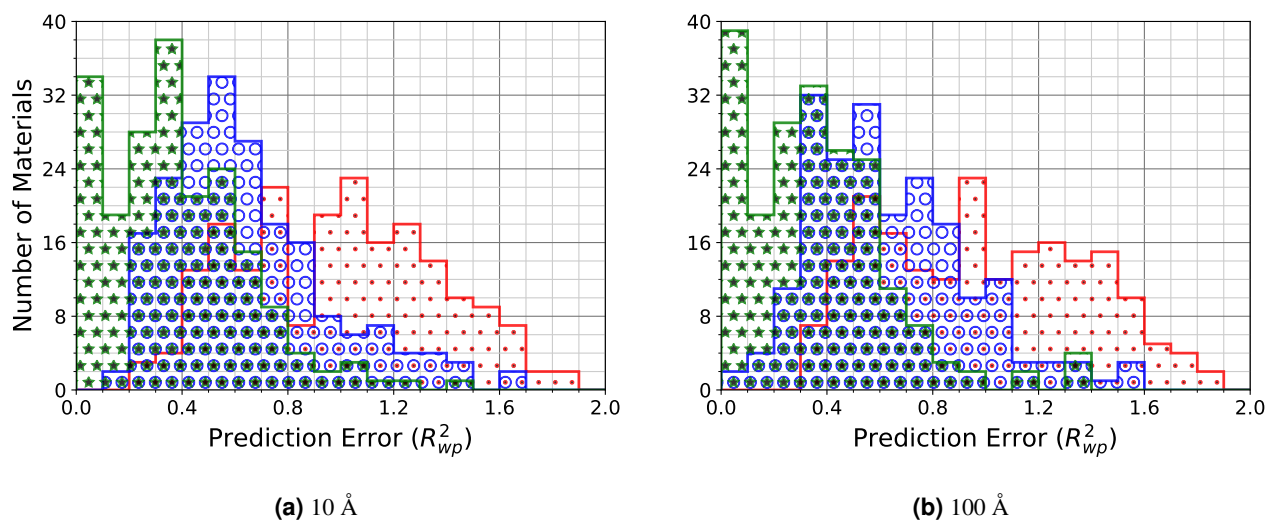


**Figure 2. Histogram (Distribution) of  $R_{wp}^2$ :** Corresponds to  $R_{wp}^2$  results shown in Table 1. The horizontal axis is  $R_{wp}^2$  (the R-factor), *i.e.*, the relative error between the predicted material's PXRD pattern and the ground truth material's PXRD pattern. The vertical axis is the number of materials from the testing set that had  $R_{wp}^2$  at a certain level. The green line with stars represents PXRNET candidates, the blue line with circles represents latent space search candidates, and the red line with dots represents random baseline candidates. Panel A is from PXRD patterns from 10  $\text{\AA}$  nanomaterials; Panel B is from PXRD patterns from 100  $\text{\AA}$  nanomaterials.

fractional coordinates of atoms in the unit cell. We have trained separate models for each nanocrystalline size, for a total of two models. We also have two baseline models (which are really ablations on PXRDNET): (1) *Latent Space Search*, which searches and decodes a trained diffusion model's latent space for materials that adhere to the PXRD pattern, *without* using any PXRD conditioning to generate the initial latent codes (2) *Semi-Random*, which creates a population of unit cells with random atomic positions and lattice parameters, and filters this population by adherence to the PXRD pattern. See Methods for more details.

See Figures 3, 4, and 5 for representative structure predictions and Table 1 for success metrics. In reviewing our results, we emphasize that the nanostructure problem currently has no end-to-end solution in the literature.

## Qualitative Analysis

Figures 3, 4, 5 show a representative sampling of PXRDNET outputs. We selected the solutions to put into Figures 3, 4, and 5 by uniformly sampling materials from PXRDNET's testing set. Thus, the spread of success and failure across these figures is roughly reflective of success and failure across the whole testing dataset. In this qualitative analysis we sorted these into ones that visually appear to be successes, partial successes and failures.

We look to Figure 3 for representative success cases. We see PXRDNET can succeed across materials with a wide variety of inorganic chemical compositions, ranging from  $\text{Sr}_2\text{MnWO}_6$  to  $\text{TeSe}_2$ . We also see that performance is similar, whether we have 10 Å or 100 Å simulated crystalline size. In particular, PXRDNET is generally successful at capturing diverse lattice shapes, such as those of  $\text{GaAgSeS}$  and  $\text{LiSc}_2\text{Rh}$ . Furthermore, we see that PXRDNET can capture symmetries in cases like  $\text{Rb}_2\text{LiMoCl}_6$  and  $\text{Tm}(\text{TiGa}_2)_2$ . In fact, even in cases like  $\text{Sr}_2\text{MnWO}_6$  (10 Å) or  $\text{LiSc}_2\text{Rh}$  (100 Å), PXRDNET does learn the correct symmetries, since the underlying graph neural network architecture is translation and rotation-equivariant, it outputs a shifted version of the unit cell. In these cases, the supercell depiction shows that the periodic structure is still correct. We note that our model is not learning symmetries present in the structure, but rather relative atomic positions in a unit cell, and so the concept of special positions is lost and the model can place the origin of the structure anywhere in the unit cell resulting in an equivalent structure.

Figure 4 shows some semi-successful cases. In many of these examples, there is still merit to PXRDNET's predictions, even if they are not fully correct. For instance, the prediction for  $\text{Hf}(\text{AlNi}_4)_4$  from the 100 Å PXRD pattern actually has an approximately correct placement of atoms within the unit cell, it is just that the identities of atoms in each particular site are wrong, *e.g.*, Hf seems to be swapped with one of the Al atoms. A similar observation holds for  $\text{Er}(\text{Al}_2\text{Cu})_4$  (100 Å). It is also worth noting that the input representation of PXRDNET does not explicitly encode when atoms are part of compounds like  $\text{AlNi}_4$ ; it may be worth investigating in the future if encoding this relation would lead to better predictions, if this information is known *a priori*. Another common failure mode is predicting the correct pattern of atoms, but within an incorrect lattice shape, as for  $\text{Li}_2\text{MnCoO}_4$  (100 Å). There are also some cases where there is a partially correct structural motif – such as the linear arrangement of the K (purple) atoms in  $\text{KNaNdTaO}_5$  (100 Å). Furthermore, there are some materials with many atoms in the unit cell, like  $\text{Pr}_2\text{Al}_2\text{Co}_{15}$ , such that a small imperfection compromises the prediction.

Finally, Figure 5 shows failure cases. Here, we see a variety of mistakes from incorrect patterning (*e.g.*,  $\text{YCo}_3\text{Ni}_2$ ) to bad unit cell predictions (*e.g.*,  $\text{TbSm}$ , 10 Å and 100 Å cases). Again, some of the predictions still have their merits. For instance, there are some locally correct structural motifs, such as the rhombohedral arrangement of Zn (gray) and Ga (green) atoms in  $\text{ZnGaPS}$ . There are also some good guesses for atomic interleaving, like the predictions for  $\text{TbSm}$  that have Tb and Sm atoms in alternating "layers", even as the lattice shape is wrong. Furthermore, some of the unit cell guesses are still decent, as in  $\text{YCo}_3\text{Ni}_2$ .

## Quantitative Analysis

There is not a universally agreed upon definition of success for a structure solution. This fact has raised challenges in the field of structure prediction, where there is discussion about how many of millions of predicted "new" structures<sup>26</sup> are actually novel<sup>41</sup>, and likewise<sup>42</sup> for the results of robotic high throughput syntheses<sup>21,43</sup>. This also presents a challenge for us to determine quantitatively the structures that are correct, mostly correct, or incorrect. This is made all the more difficult because structures are solved just up to isometry from powder diffraction data, and may be rotated, displaced or inverted compared to ground-truth but nonetheless correct.

In the field of structure solution from powder diffraction, a final structure refinement step is applied where a local search is carried out such that structural parameters (lattice parameters and fractional coordinates) are modified using non-linear regression methods to obtain the best fit to the measured powder diffraction pattern<sup>44</sup>. Finally, the chemical plausibility (*e.g.*, interatomic distances, bond angles, missing or extra sites in organic compounds) of the resulting structure is tested using CIF-checkers, most notably IUCr's CheckCIF<sup>45</sup>. These steps are not easily automated and are not high throughput, and so not appropriate for our purposes. They are also problematic for us because our *ab initio* approach does not first find the unit-cell with high accuracy as is done in the indexing process with high resolution powder diffraction methods. We tried the local refinement and found that the local search is very sensitive to having correct unit cell parameters, even when these are less relevant parameters for small nanoparticles that are our target here. We believe that these issues will be resolved in the future,

but rather than address them here we turn to other measures of success that are high throughput. We note that these may not accurately reflect the actual degree of success of our method. They are more likely to result in false negatives than false positives and likely under-count the success rate, though this needs to be established. The metrics are described in the "Methods" section.

The quantitative results of Table 1 support the qualitative observations and show that PXRDNET is successful at reconstructing materials in MP-20. We compare our models against the aforementioned *Latent Space Search* and *Semi-Random Search* baselines (more details in Methods). PyMatGen has a structural matching algorithm<sup>38</sup> which we ran with the default parameters, as was the procedure in many prior works<sup>22–25,28,29</sup>. This function classifies as structure as correct or not within some small angular and translational tolerances. To get the number in Table 1 we feed the top 5 candidates from PXRDNET to the PyMatGen matching algorithm. If one of the structures is successful we deem this to be a successful structure solution by this measure.

We see that PXRDNET's predictions are considerably better than the latent space search baseline, and better yet than the semi-random baseline. By this measure we can predict the correct structure almost half the time, whereas the latent space search baseline gets it right about one-fifth of the time, and the random search baseline gets virtually none of them right. The best match rate is 50.0% on the 10 Å crystalline size. This is contrary to expectations, as conventional wisdom suggests that the smaller the crystal, the higher the peak broadening, and the lower the information content in the PXRD signal<sup>2,3</sup>. While we do not wish to baselessly speculate on the reasons for this, we note that peak broadening makes for a smoother and less sparse optimization objective, which is better for machine learning, in our experience. At any rate, this is good news, because it means that the Diffusion model can make progress on a problem that was previously thought to be intractably difficult. For the 100 Å particles the results were lower but similar, sitting at 45.5% match rate.

Taking a different approach to measuring success we can compare the atomic pair distribution function (PDF) of the candidate structures to that of the ground-truth using the Pearson correlation function<sup>37</sup> as the distance metric. Here 1 implies a perfect agreement and 0 that the two curves are uncorrelated. The PDF is useful as a 1D representation of the 3D structure and is a the Fourier transform of the powder diffraction pattern<sup>4</sup>. For each material, we report the single best PDF correlation out of PXRDNET's top 5 returned candidates.

Overall, the PDF correlations of the two PXRDNET models follow the same trend as the PyMatGen match rate. The model structures significantly out-perform both the latent space and semi-random baseline models, with the latent space baseline being somewhat closer to PXRDNET's performance. When we compare the two PXRDNET models to each other, there is not that much difference, as they are all within one standard deviation of each other.

Finally, we measure  $R_{wp}^2$ , the profile-weighted R-factor, which is the intensity-weighted sum of squares of the deviation of the predicted and ground truth powder patterns (see "Methods" for details). Here, lower values are better. This measure is used as a target function in Rietveld structure refinements, whence a highly successful fit typically has  $R_{wp}^2$  below 10%<sup>3</sup>. Just as with PDF correlation, for each material, we report the single best  $R_{wp}^2$  out of PXRDNET's top 5 returned candidates.

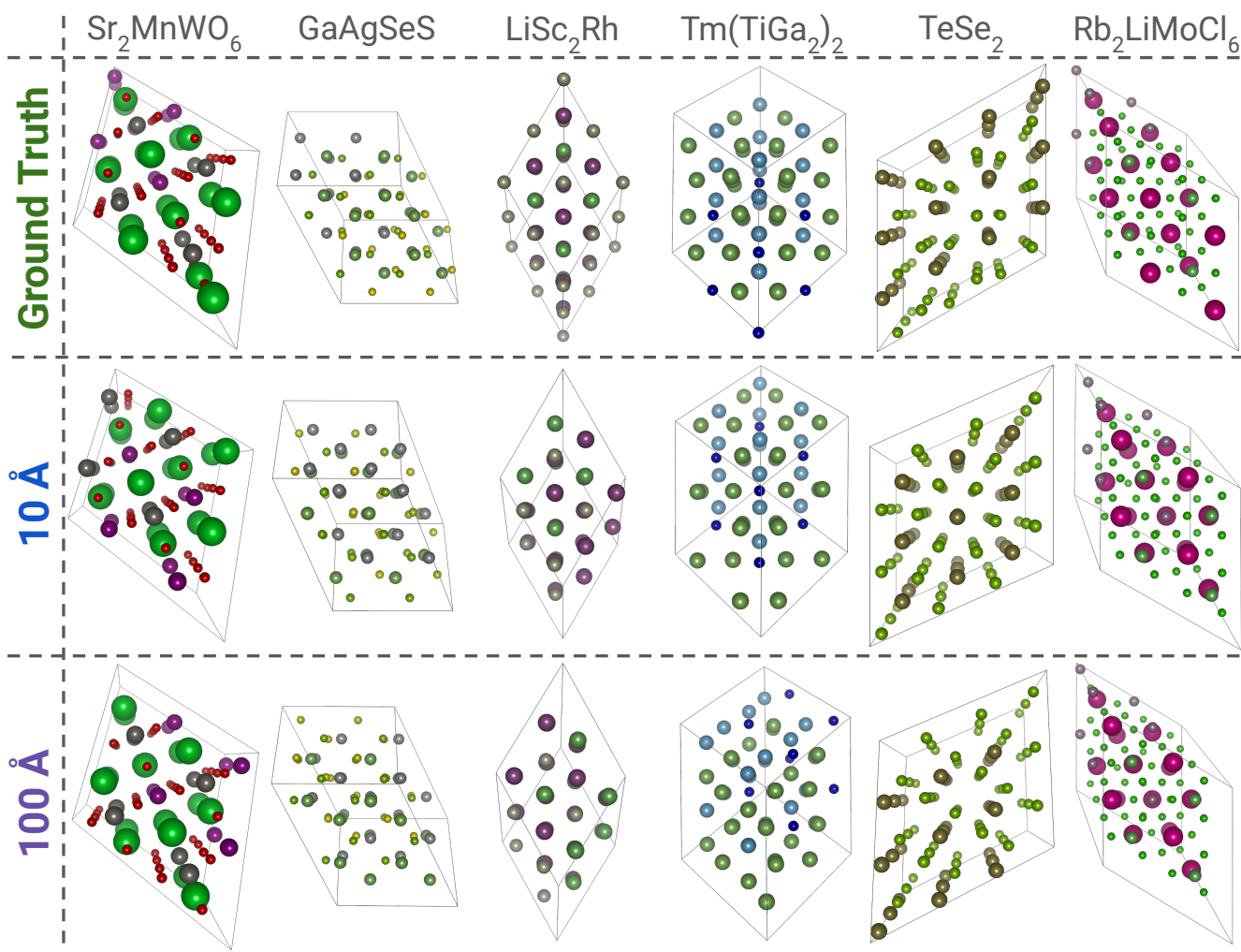
This measure should perform similarly to the Pearson measure and it does. The two PXRDNET models perform at essentially the same level, and they both considerably outperform both the baseline models. Before model refinement, even from conventional structure solution methods from well crystallized samples, this measure can be considerably higher than 10%, even for the correct structure. This shows that our method, while far from perfect, can give decent structural candidates for a considerable number of materials.

Figure 2 shows the distribution of  $R_{wp}^2$  for PXRDNET (green), the latent search baseline (blue), and the random search baseline (red). We see that for both PXRDNET models, the peaks of the distributions are concentrated around relatively low  $R_{wp}^2$ , many below 10%, with rightward tails representing higher  $R_{wp}^2$ . In contrast, the latent search baselines peak at higher  $R_{wp}^2$ , with very few of their  $R_{wp}^2$  crossing the 10% threshold. Similarly to the PXRDNET distribution, the latent search distribution is also somewhat right-skewed. Finally, the random search baselines have the highest  $R_{wp}^2$  of all, with very little skew. This highlights the advantages of diffusion models in finding plausible structural candidates, and further emphasizes the power of PXRDNET specifically in generating high-quality structural candidates.

## Comparison Across Crystal Systems

Especially with information diminished inputs, more complex structures are harder to solve. This was seen in the recent study where *CrystalNet*, a generative AI encoder-decoder, was considerably more successful on simpler materials from cubic crystal systems<sup>30</sup>. To investigate this in the current case, the performance of PXRDNET is broken out by crystal system in Table 2, where the results are from the same experimental run as Table 1.

Unsurprisingly, and in line with previous work<sup>30</sup>, we find that the cubic system is the easiest to solve, with match rates up to 80.8% (as compared to a sub-50% overall match rate). This trend holds, regardless of nanomaterial crystal size. We also find that different nanomaterial crystal sizes are better suited for different crystal systems. For instance, the 10 Å size does very well on the orthorhombic and the tetragonal systems (which both have 90° lattice angles), predicting the correct material above 50% of the time by this measure, while the baseline models do not reach this level of success. Then, the 100 Å crystal size gives



**Figure 3. PXRNET Successful Cases:** The leftmost column is the ground truth crystal structure. The other columns show PXRNET’s reconstructed crystal structures from simulated nanocrystal PXR patterns of diameter 10, 100 Å. For convenient visualization of some examples, we have tessellated their unit cells into super cells. We selected the solutions to put into Figures 3, 4, and 5 by uniformly sampling materials from PXRNET’s testing set. Thus, the spread of success and failure across these figures is roughly reflective of success and failure across the whole testing dataset.

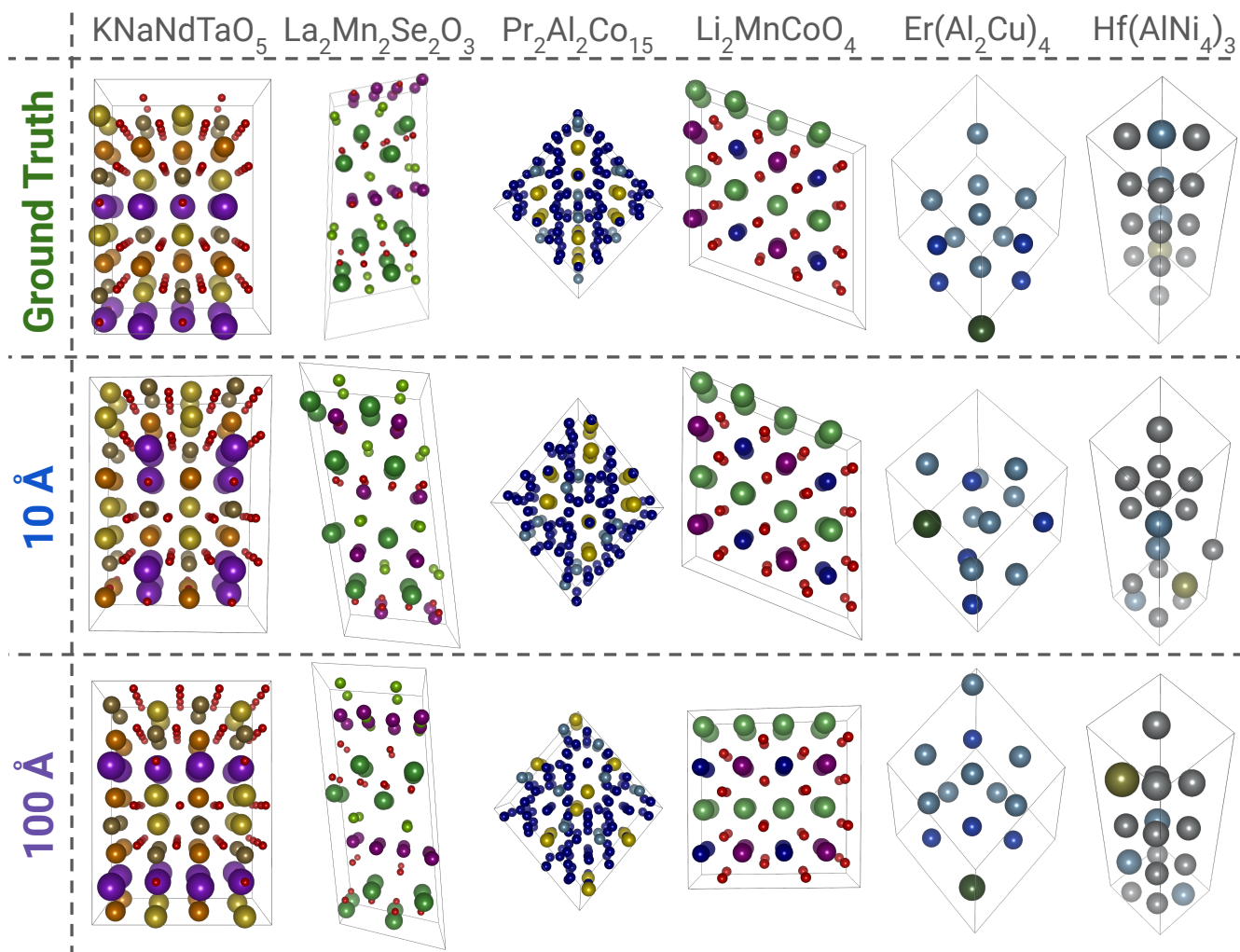


**Figure 4. PXRNET Semi-Successful Cases:** The leftmost column is the ground truth crystal structure. The other columns show PXRNET’s reconstructed crystal structures from simulated nanocrystal PXR patterns of diameter 10, 100 Å. For convenient visualization of some examples, we have tessellated their unit cells into super cells. We selected the solutions to put into Figures 3, 4, and 5 by uniformly sampling materials from PXRNET’s testing set. Thus, the spread of success and failure across these figures is roughly reflective of success and failure across the whole testing dataset.

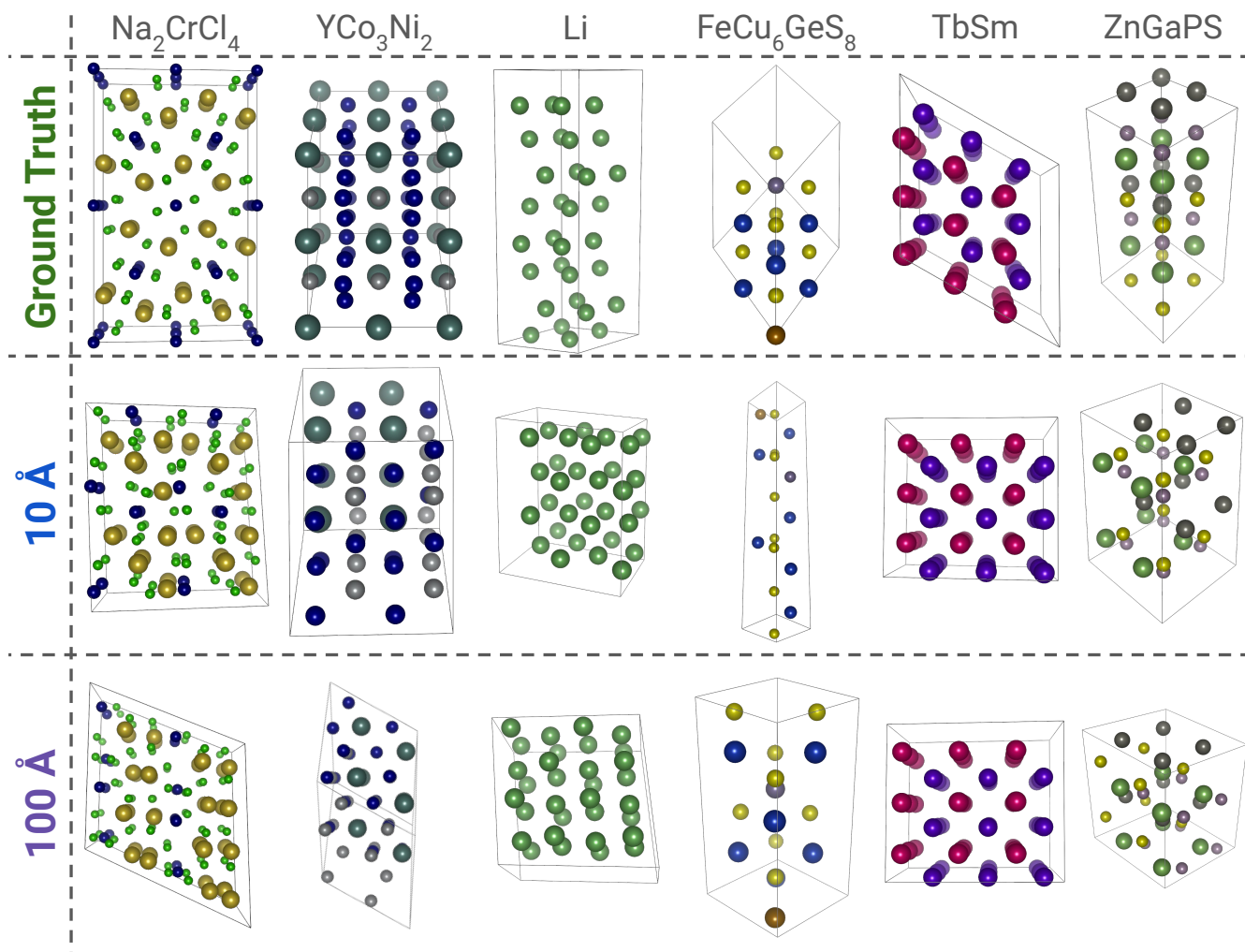


**Figure 5. PXRDNET Unsuccessful Cases:** The leftmost column is the ground truth crystal structure. The other columns show PXRDNET’s reconstructed crystal structures from simulated nanocrystal PXRD patterns of diameter 10, 100 Å. For convenient visualization of some examples, we have tessellated their unit cells into super cells. We selected the solutions to put into Figures 3, 4, and 5 by uniformly sampling materials from PXRDNET’s testing set. Thus, the spread of success and failure across these figures is roughly reflective of success and failure across the whole testing dataset.



Crystal System (#)	PXRDNET (10 Å)	PXRDNET (100 Å)	Latent Search (10 Å)	Latent Search (100 Å)
<b>Match Rate (↑)</b>				
Cubic (52)	0.769	0.788	0.481	0.481
Tetragonal (31)	0.516	0.419	0.097	0.258
Orthorhombic (35)	0.571	0.371	0.086	0.057
Trigonal (23)	0.391	0.348	0.130	0.000
Hexagonal (12)	0.250	0.417	0.000	0.167
Monoclinic (37)	0.297	0.270	0.054	0.108
Triclinic (10)	0.100	0.100	0.000	0.000
<b>PDF Correlation (↑)</b>				
Cubic (52)	0.834 ± 0.12	0.834 ± 0.15	0.630 ± 0.10	0.668 ± 0.12
Tetragonal (31)	0.773 ± 0.08	0.762 ± 0.11	0.690 ± 0.09	0.681 ± 0.08
Orthorhombic (35)	0.796 ± 0.10	0.790 ± 0.12	0.719 ± 0.09	0.717 ± 0.08
Trigonal (23)	0.778 ± 0.11	0.781 ± 0.11	0.695 ± 0.08	0.681 ± 0.09
Hexagonal (12)	0.725 ± 0.12	0.721 ± 0.10	0.695 ± 0.06	0.691 ± 0.07
Monoclinic (37)	0.796 ± 0.10	0.774 ± 0.10	0.746 ± 0.09	0.741 ± 0.09
Triclinic (10)	0.841 ± 0.04	0.828 ± 0.05	0.788 ± 0.07	0.793 ± 0.05
<b>R<sub>wp</sub><sup>2</sup> (↓)</b>				
Cubic (52)	0.692 ± 0.54	0.600 ± 0.54	1.745 ± 0.41	1.674 ± 0.41
Tetragonal (31)	0.997 ± 0.42	1.024 ± 0.55	1.434 ± 0.40	1.484 ± 0.47
Orthorhombic (35)	0.820 ± 0.39	0.818 ± 0.48	1.176 ± 0.43	1.159 ± 0.49
Trigonal (23)	0.880 ± 0.36	0.983 ± 0.52	1.386 ± 0.48	1.338 ± 0.36
Hexagonal (12)	1.173 ± 0.33	1.238 ± 0.40	1.312 ± 0.30	1.355 ± 0.30
Monoclinic (37)	0.720 ± 0.33	0.808 ± 0.51	1.205 ± 0.53	1.143 ± 0.55
Triclinic (10)	1.034 ± 0.51	1.083 ± 0.55	1.215 ± 0.36	1.141 ± 0.40

**Table 2. Results by Crystal System:** *Crystal System (#)* refers to the crystal system name, and the number of materials we have in the dataset of that system. Interpretation of metrics and method names remains the same as Table 1. All results shown are for MP-20. Because the semi-random baseline is so poor, we omit it, and only show the latent space search baseline with PXRDNET.

good results for hexagonal. The success rate does decrease with decreasing symmetry of the structure, with the triclinic crystal system performing the least well according to the PyMatGen metric. However, we note that this trend is much less apparent when looking at the PDF correlation as a metric. The PDF is more sensitive to the relative positions of atoms than to crystal symmetry. In this sense the PDF may be a better measure of success for small nanocrystals and atomic clusters. For the PDF metric there is less clear of a trend from higher symmetry to lower symmetry ground-truth structure. Caution must be exercised here due to there being only 10 triclinic materials in the testing set.

### Performance with Experimental PXRD Patterns of Real-World Materials

Finally, we test on a small number of experimentally determined PXRD patterns. The patterns were obtained from IUCr's database<sup>46</sup>. We did artificially induce sinc and Gaussian filters (*i.e.*, simulated nanoscale) on these patterns before feeding them into our model, to make them consistent with the training data that did undergo such filters. See "Methods" for more details.

Encouragingly, we find that PXRDNET overcomes the simulation-to-real gap, in that its success, as measured by both visual analysis (Figures 6, 7, and 8) and quantitative metrics (Table 1), are comparable to those obtained from the simulated data. We can see that the experimental PXRD patterns are of variable quality. Yet, there are many success cases like BaTiO<sub>3</sub> (Figure 8), AlPO<sub>4</sub>, and LaInO<sub>3</sub> (Figure 6). That being said, we do observe that some lattice parameters are very obviously wrong, such as in C<sub>4</sub>SBr<sub>4</sub> (Figure 6), ErGe<sub>2</sub>, EuI<sub>2</sub> (Figure 7), and KLaTiO<sub>4</sub> (Figure 8).

### Test of structure refinement step

In light of the discussion above about model refinement as a final step in conventional structure solution, we attempted a Rietveld refinement on a subset of 20 candidates from PXRDNET.

Figure 9 shows  $R_{wp}^2$  values for these candidates before and after the Rietveld refinement step. The Rietveld refinement works well for the 100 Å test cases, which have sharper Bragg peaks. Except for four cases, the refinement brought  $R_{wp}^2$  below 20%. There may still be some issues with the structure in these cases, but PXRDNET is clearly returning structures that are quite similar to the true one and possibly close enough to yield a correct structure with some human input in each case.

We note that the average unrefined  $R_{wp}^2$  of this sampling of materials were actually worse than the unrefined  $R_{wp}^2$  of the materials in the overall testing set (0.526 vs. 0.377 for 10 Å crystals; 0.478 vs. 0.364 for 100 Å crystals). The subset of targets we chose for refinement are not best-case or even average-case, and we might expect Rietveld refinements on wider ranges of targets would perform better than this sampling on average.

The Rietveld refinements were much less successful for the 10 Å nanoparticles, which have highly distorted diffraction patterns. In many cases the refinement resulted in a worse  $R_{wp}^2$ , indicating that the refinements were not converged and not stable.

This aspect of the work can be developed in the future, with better understanding of how to refine structural models in a more automated way, either against the PDF or against powder data, to obtain a higher structure solution rate.

## Discussion

The Diffusion model implemented in PXRDNET provides an exciting step towards structure solution from information compromised input data such as would come from nanomaterials. As an end-to-end method to solve nanostructures from information-compromised diffraction data, it is easy to use.

As with any structure solution method, we do not expect 100% success but seek a method that can provide structural candidates that may be further assessed for their validity. In this regard PXRDNET has shown a high capability due to the inherent stochasticity of Langevin dynamics<sup>35</sup>, which results in multiple structural candidates.

More work will be needed to understand exactly the ways that the structures fail, for example, in terms of incorrect geometry vs. chemical switches, and we believe that novel refinement methods can be developed that are better tuned to error correction in PXRDNET generated structures than is Rietveld refinement.

We find it interesting that PXRDNET actually works very well, if not better, in cases where the information content was previously thought to be lower, *e.g.*, 10 Å nanocrystal size. This provides an optimistic note for future computational crystallographic and materials science research, as it shows that problems that are harder for humans are not necessarily harder for data-driven and machine learning methods.

Finally, we note that while we evaluated on PXRD data, in principle, models could be trained to work on diffraction data coming from other popular modalities like electron or neutron diffraction.

### Limitations and Future Work

One limitation of our model is that it requires *a priori* knowledge of the chemical formula. While this is a reasonable assumption in crystallography<sup>3,4,30</sup>, it would be even more powerful if, given partial or even no information about the chemical composition,

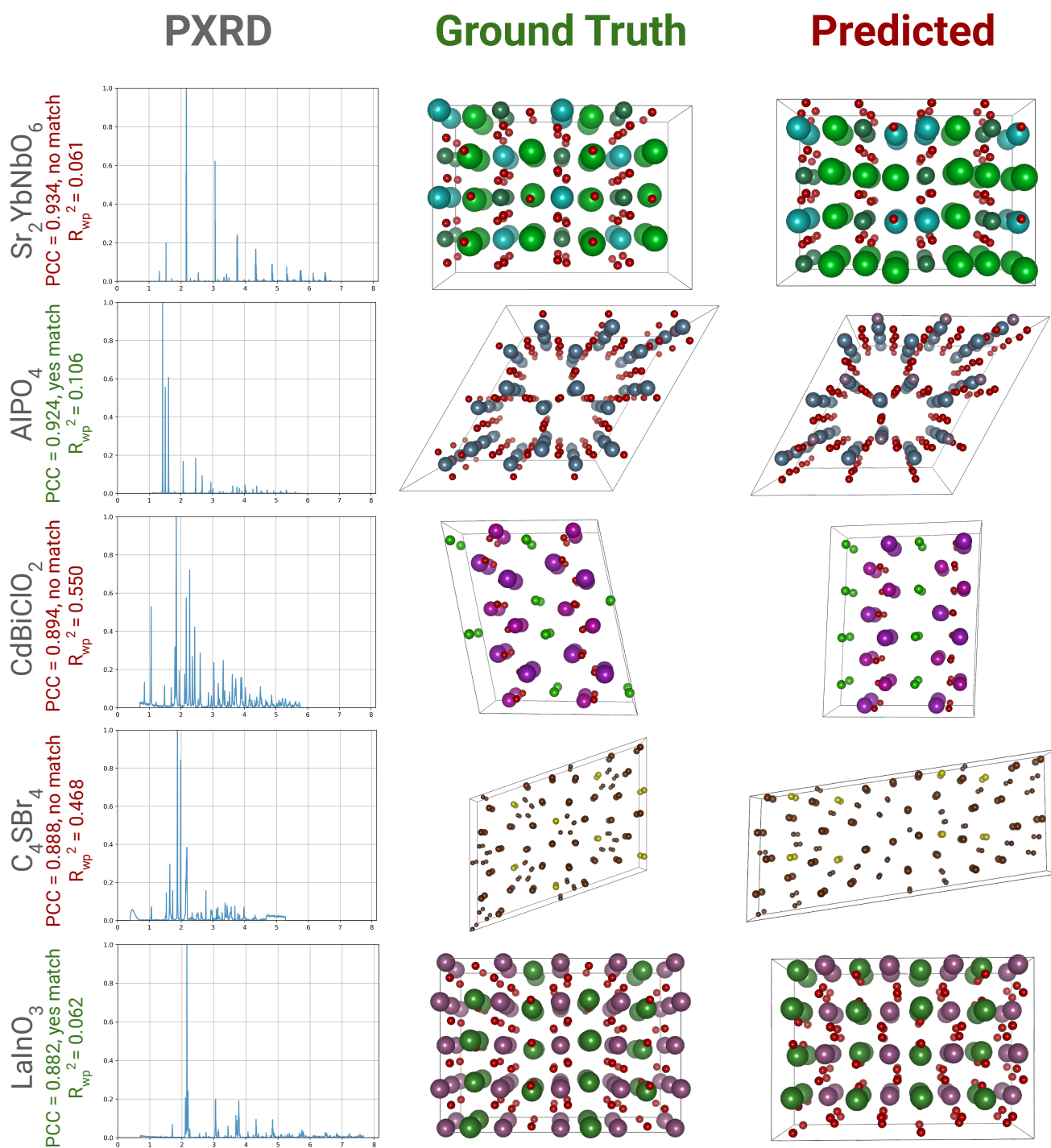


**Figure 6. Experimental Data:** The leftmost column is the experimentally observed PXRD pattern, where the horizontal axis is  $Q$  ( $\text{\AA}^{-1}$ ), and the vertical axis is the scaled intensity of the pattern. The middle column is the ground truth crystal structure. The rightmost column is the predicted crystal structure. For convenient visualization of some examples, we have tessellated the unit cells. The labels are the chemical formula, Pearson's correlation<sup>37</sup> between ground truth and simulated pair distribution functions, whether or not PyMatGen<sup>38</sup> determined the predicted structure to match the ground truth, and  $R_{wp}^2$ .

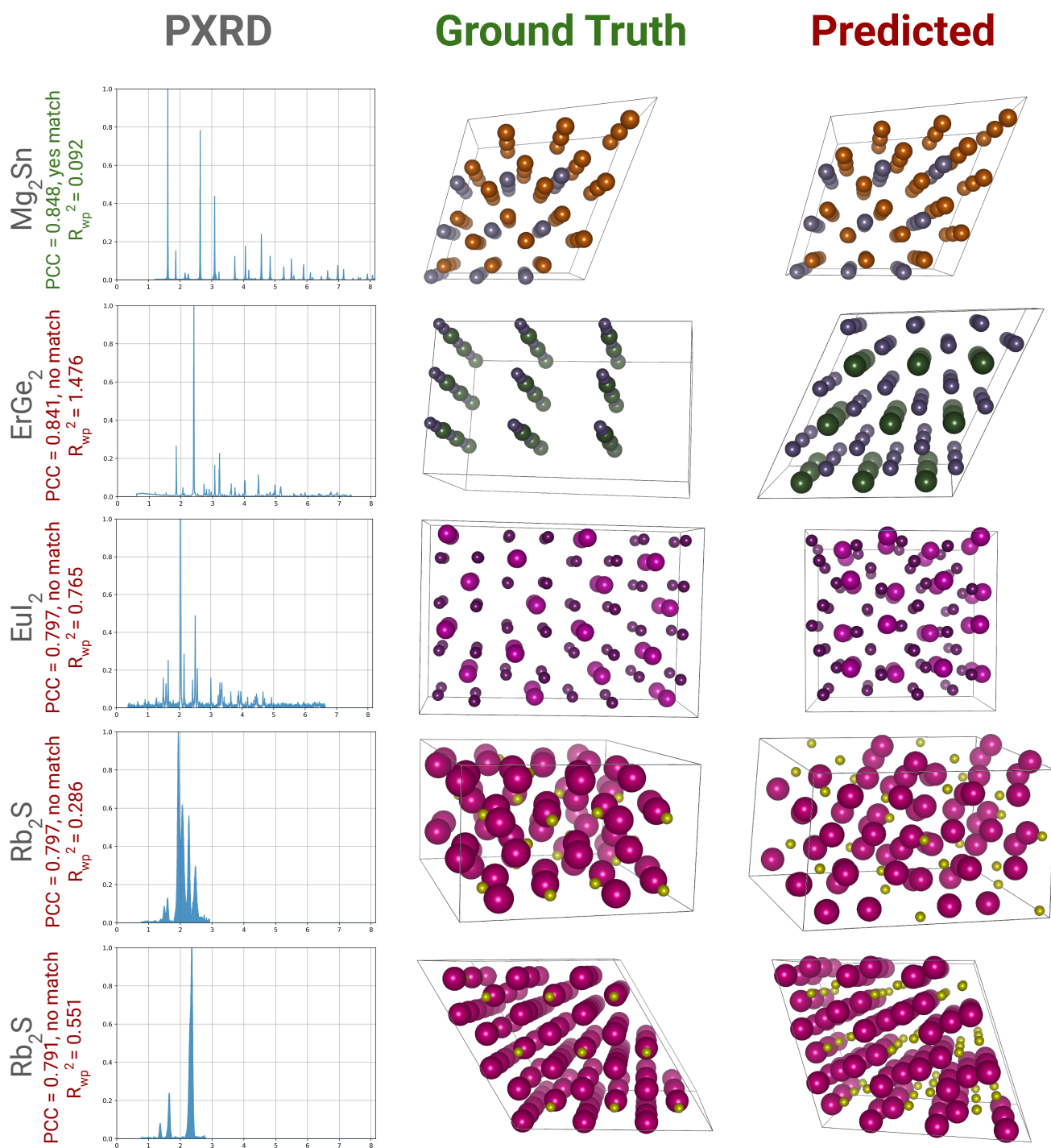


**Figure 7. Experimental Data (Cont.):** The leftmost column is the experimentally observed PXRD pattern, where the horizontal axis is  $Q(\text{\AA}^{-1})$ , and the vertical axis is the scaled intensity of the pattern. The middle column is the ground truth crystal structure. The rightmost column is the predicted crystal structure. For convenient visualization of some examples, we have tessellated the unit cells. The labels are the chemical formula, Pearson's correlation<sup>37</sup> between ground truth and simulated pair distribution functions, whether or not PyMatGen<sup>38</sup> determined the predicted structure to match the ground truth, and  $R_{wp}^2$ .

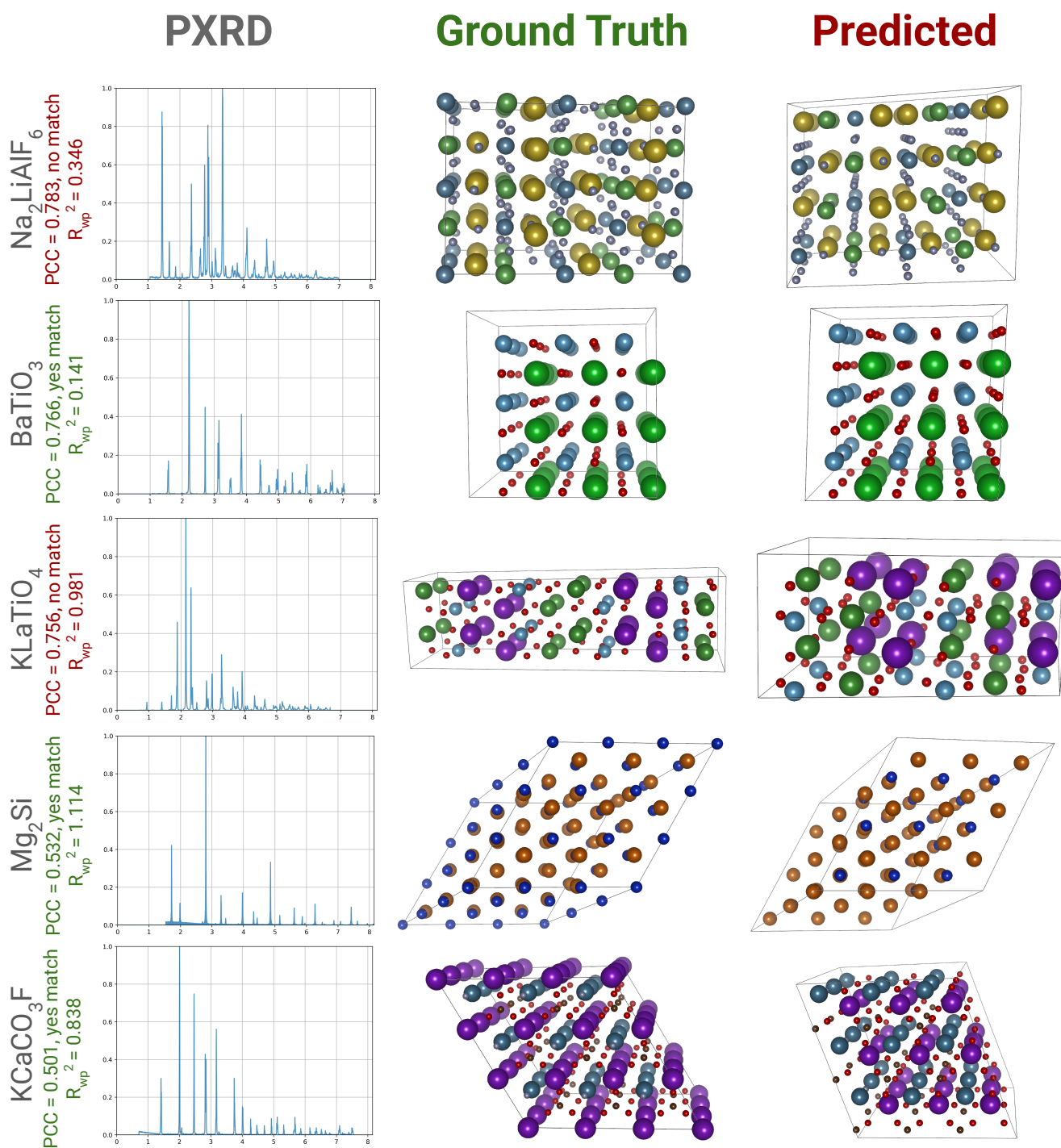


**Figure 8. Experimental Data (Cont.):** The leftmost column is the experimentally observed PXRD pattern, where the horizontal axis is  $Q(\text{\AA}^{-1})$ , and the vertical axis is the scaled intensity of the pattern. The middle column is the ground truth crystal structure. The rightmost column is the predicted crystal structure. For convenient visualization of some examples, we have tessellated the unit cells. The labels are the chemical formula, Pearson's correlation<sup>37</sup> between ground truth and simulated pair distribution functions, whether or not PyMatGen<sup>38</sup> determined the predicted structure to match the ground truth, and  $R_{wp}^2$ .

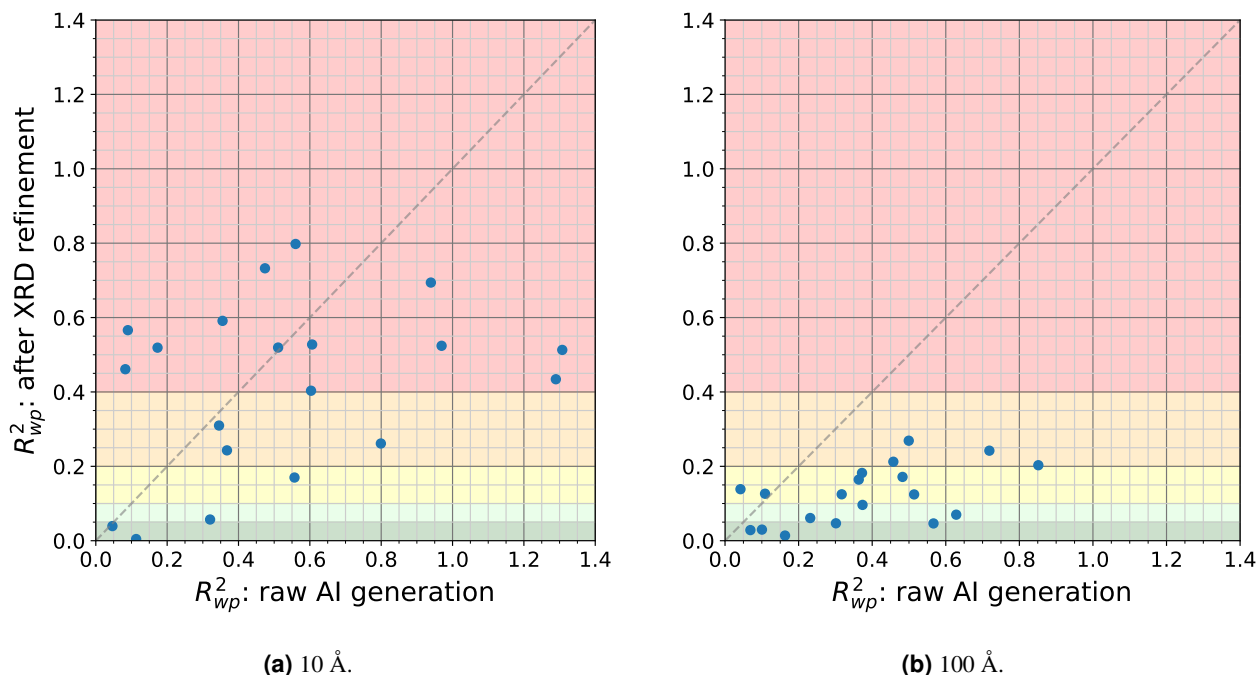


**Figure 9. Rietveld Refinement Results:** We conducted Rietveld refinement on 20 materials. Panel A shows the results for 10 Å nanocrystal size; Panel B shows the results for 100 Å nanocrystal size. The horizontal axis is the calculated  $R_{wp}^2$  before refinement; the vertical axis is the calculated  $R_{wp}^2$  after refinement. One outlier ( $\sim 2.4, \sim 0.05$ ) is excluded from Panel B. For 10 Å nanocrystal size, pre-refinement  $R_{wp}^2$  has  $\mu \pm \sigma = 0.526 \pm 0.367$ , and post-refinement  $R_{wp}^2$  has  $\mu \pm \sigma = 0.418 \pm 0.224$ . For 100 Å nanocrystal size, pre-refinement  $R_{wp}^2$  has  $\mu \pm \sigma = 0.478 \pm 0.490$  (including outlier), and post-refinement  $R_{wp}^2$  has  $\mu \pm \sigma = 0.119 \pm 0.075$  (including outlier).

our model could still solve structures, and this will be explored. Another limitation of our current work is that materials from MP-20 have at most 20 atoms in the unit cell<sup>28</sup>. This covers a wide range of useful materials, but many important materials have many more atoms in the unit cell. Scaling up our approach to materials with more atoms in the unit cell will also be the subject of future work.

On the other hand, the data quality that was used in this study was low. Powder patterns were used over a limited range to  $Q < 8.2 \text{ \AA}^{-1}$  and broadened because of the nanoparticle sizing. In practice, it is often the case that real data available, for example, from x-ray synchrotron sources, has more information than the patterns that were used in this first test. Training models that work on higher quality diffraction patterns can be expected to extend the quality of structure predictions from PXRDnet.

The model is already out-performing in terms of structural complexity earlier attempts at nanoparticle structure solution<sup>5,6,47</sup> and more refinements to the approach are eminently possible.

## Methods

### Dataset

#### Materials Project: MP-20-PXRD

We used the MP-20 dataset of the Materials Project<sup>36</sup> which consists of materials sampled from the Materials Project database with at most 20 atoms in the unit cell<sup>28</sup>. Powder diffraction patterns for all structures in MP-20 were simulated using the PyMatGen package<sup>38</sup>. Our simulation uses CuK $\alpha$  radiation with  $Q$  values ranging from  $0 \leq Q \leq 8.1568 \text{ \AA}^{-1}$ .

The files are made available as a dataset we call MP-20-PXRD which we include with our open source code. We hope that this will encourage the computational material science community to extend our work and explore the structure solution from PXRD problem even more.

We use MP-20-PXRD to train PXRDNET end-to-end. MP-20-PXRD contains 45,229 materials, and we use a 90-7.5-2.5% train-val-test split.

### Experimental PXRDs

We obtained 15 experimental patterns from searching IUCr’s database<sup>46</sup>. The difficulty in procuring experimentally gathered PXRDs *en masse* is that the reporting format for such patterns is not standardized. There is a powderCIF<sup>48</sup> format to standardize this but few authors deposit their powder data in this form, if at all. Furthermore, even among the diffraction patterns available, many are from other scattering sources, like neutron diffraction. In future works, we plan to more systematically and extensively curate experimental PXRD patterns. It would be very helpful if powder patterns were deposited in a standard format with published papers.

We also use the 10 Å filter and Gaussian broadening on the experimental PXRD data, to make the patterns consistent with what was seen during train time by our model.

### Finite size effects

To model the nano-scale finite size of the particles we assumed the diffraction pattern to be that of a long-range ordered crystal, convoluted with the Fourier transform of a window function on the PDF,

$$\Pi(r/\tau) = \begin{cases} 0 & |r| > \frac{\tau}{2} \\ \frac{1}{2} & |r| = \frac{\tau}{2} \\ 1 & |r| < \frac{\tau}{2} \end{cases} \quad (1)$$

where  $r$  is the interatomic distance and  $\tau$  is the nanomaterial width. We therefore convolute the diffraction pattern with its Fourier transform,

$$\mathcal{F} \left\{ \Pi \left( \frac{r}{\tau} \right) \right\} = \tau \frac{\sin \left( \frac{Q\tau}{2} \right)}{\frac{Q\tau}{2}} \quad (2)$$

where  $Q$  is the magnitude of the scattering vector<sup>4</sup>. The result of the convolution can be seen in Figure 1.

Simulating nanoscale shrinkage effects for *larger* nanomaterial widths requires sampling from increasingly high frequency sinc functions. As a result, discrete sampling from these signals requires a large sampling rate to avoid any aliasing effects. To that end, we simulate PXRD patterns as scalar-valued functions over 4096 evenly sampled points in the range 0 to 8.1568 Å<sup>-1</sup>, resulting in a sampling rate of 502.16 Å. By the Nyquist Sampling Theorem<sup>49</sup>, this sampling rate limits the bandwidth of any signal of interest (that is, the sinc pattern) to 251.08 Å to avoid aliasing effects. All the sinc functions we use have maximum frequency below this sampling rate.

The convoluted diffraction pattern is then downsampled to the 512 input samples expected by PXRDNET.

After simulating nanoscale shrinkage, we also apply Gaussian smoothing with  $\sigma$  ranging uniformly between 0.081568 Å<sup>-1</sup> and 0.0897248 Å<sup>-1</sup>. Empirically, we found this improved PXRDNET performance – we believe that the smoothing produces more continuous regression targets for the PXRD-regressor.

We train and test a separate model for each crystal size (10 Å, 100 Å).

### Base Model: Hybrid Diffusion-VAE

PXRDNET builds off of CDVAE (Crystal Diffusion Variational Autoencoder), a previously proposed material structure generative model<sup>28</sup>. The CDVAE model unconditionally generates materials represented by a graph encoding of the following tuple of characteristics: a list of atom types  $\mathbf{A} \in \mathbb{R}^N$ , a list of atom coordinates  $\mathbf{X} \in \mathbb{R}^{N \times 3}$ , and a periodic lattice  $\mathbf{L} \in \mathbb{R}^{3 \times 3}$  where  $N$  is the number of atoms in the unit cell. Concretely, the model decodes material composition and structure from randomly sampled noise via a diffusion process. By training on a diverse set of observed material structures, CDVAE learns to capture the underlying distribution of physically stable materials.

At a high level, the idea behind CDVAE is adopted from the variational autoencoder<sup>50</sup> and denoising diffusion networks<sup>51</sup>, which are generative models that learn to decompress data from noise. Essentially, such models are trained to encode data  $x$  to a latent representation  $z$ , then map it back to the original space to produce a reconstructed version of the original data sample  $x$ . The latent representation  $z$  is regularized such that the distribution  $p(z)$  looks roughly like a standard normal distribution over the latent space. At inference time, generating samples simply involves sampling from  $N(0, I)$  and decoding to the original data domain.

Implementationally, CDVAE is a hybrid between the noise-conditioned score network (the diffusion model) and the variational autoencoder (VAE). To understand the breakdown of the VAE and diffusion components, recognize that the unit cell of a material can be represented by four components: (1) chemical composition, (2) number of atoms, (3) lattice parameters, (4) atomic coordinates. CDVAE’s first branch addresses components (1)-(3) with a variational autoencoder. The encoder is DimeNet<sup>52</sup>, an SE(3)-invariant graph neural network that maps the graph representation of a material to a latent representation  $z$ . The graph representation has been modified to be a directed multi-graph that respects the inherent periodicity of materials<sup>53</sup>.

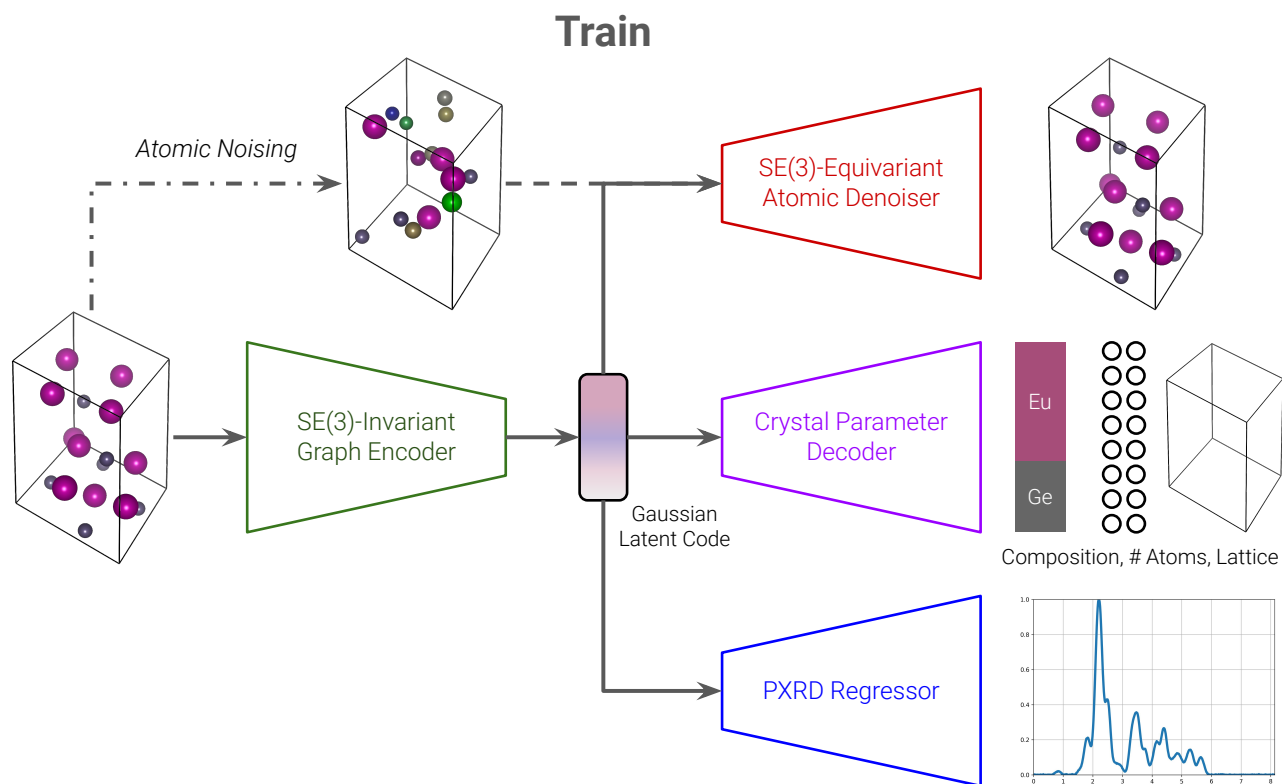


**Figure 10. PXRNET's Training Process:** PXRNET's training process essentially follows that from CDVAE. The objective is twofold: (1) to learn how to reconstruct the material after a noising process; (2) predict PXRD patterns from a compressed material representation. To this end, it has three branches: denoising diffusion of atomic species and coordinates (via "SE(3)-Equivariant Atomic Denoiser"); variational autoencoding of composition, number of atoms, and lattice parameters (via "Crystal Parameter Decoder"); and PXRD regression (via "PXRD Regressor"). These branches are all connected via the common Gaussian latent code (generated from "SE(3)-Invariant Graph Encoder").



The latent representation,  $z$ , is regularized to be a multivariate Gaussian, via the Kullback–Leibler-divergence loss<sup>50</sup>. Then, from  $z$ , it decodes (1) the chemical composition (as ratios), (2) the number of atoms, and (3) the lattice parameters ( $a$ ,  $b$ ,  $c$ ,  $\alpha$ ,  $\beta$ ,  $\gamma$ ). Each prediction is produced by a separate crystal parameter multi-layer perceptron that takes in the latent encoding  $z$ . This latent code  $z$  is especially important, as it is later used as the material representation in all the other branches of the model, as described below.

CDVAE’s second branch addresses component (4) with denoising diffusion via noise conditioned score networks<sup>35,54</sup>. It assumes that components (2)-(3) – the number of atoms and lattice parameters – are fixed. The forward process perturbs the atomic coordinates and atomic species with multivariate Gaussian noise. The reverse process is parameterized by GemNet<sup>55</sup>, an SE(3)-equivariant graph neural network. It is conditioned on the latent code,  $z$ , from the aforementioned material graph encoding; thus, it is crucial to learn an informative  $z$  in the VAE branch in order for this diffusion branch to work. The reverse process essentially predicts how to denoise the perturbed atomic coordinates and species via annealed Langevin dynamics, such that they move to their true positions and revert to their true species<sup>35</sup>. Again, the output graph representation is a directed multi-graph that is compatible with the periodic nature of materials<sup>53</sup>.

Then, at generation time, CDVAE generates materials as follows: First, sample a latent code  $z \sim N(0, I)$  from the multivariate Gaussian distribution. This is decoded with the aforementioned crystal parameter MLPs to gain components (1)-(3): the lattice parameters, chemical composition, and number of atoms. This can be used to initialize a unit cell, where the atomic positions are randomly chosen, again from  $N(0, I)$ . Then, the atomic positions and species are refined through the Langevin dynamics SE(3)-equivariant graph denoising process, which is also conditioned on the latent code  $z$ . Note that the lattice parameters and number of atoms stay fixed throughout the denoising process. This yields the generated material.

A natural question that arises is, why is it necessary to have both VAE and denoising diffusion components? The rationale for using denoising diffusion is that, when predicting atomic coordinates, it actually has a theoretical connection to harmonic forcefields<sup>28</sup>. Furthermore, denoising diffusion has achieved high performance in other generative tasks<sup>35,54</sup>. However, the VAE portion is still necessary, because the traditional formulation of denoising diffusion<sup>35,51,54</sup> requires a fixed data representation dimensionality. In this case, the dimensionality of the data representation is (some multiple of) the number of atoms, so that cannot be denoised. To get around this, the VAE branch predicts the number of atoms, which is then used to initialize the denoising diffusion.

For additional details, including training loss functions, input and output representations, and hyperparameters, we refer the reader to the original CDVAE paper: we adopt most of their settings, unless specified otherwise<sup>28</sup>. Also, refer to Figure 10 for a schematic diagram of the training process for our CDVAE-inspired model.

## Property Optimization

As an additional feature, CDVAE includes property optimization, which allows one to steer the generative process towards materials with desired properties. A differentiable property predictor (implemented as a neural network) is trained to regress the desired property from the latent molecule representation  $z$ . To bias generation towards molecules with the desired property at inference time, gradient descent is used to adjust  $z$  (while the property predictor is frozen) to achieve the desired predicted property value. The optimized  $z$  is then used to initialize the material structure, and is further passed as conditioning to the atomic denoising process, as previously described.

## PXRD Regressor Architecture

In our setting, the PXRD pattern is the desired property to predict. Thus, we design a PXRD Regressor  $F_\psi$  that maps from PXRDNET’s latent material representations  $z \in \mathbb{R}^{256}$  to a vector  $y \in \mathbb{R}^{512}$ , the estimated  $Q$ -space representation of the material’s PXRD pattern. The PXRD Regressor is parameterized by a DenseNet-inspired architecture<sup>56</sup>, which extends traditional convolutional neural networks. We base our regressor off of the design in *CrystalNet*<sup>30</sup>, which has a densely connected architecture with 1D inputs and outputs. Concretely, for a given depth in the network DenseNet aggregates previous intermediate data representations as input to the next convolutional layer. DenseNet has been shown to reduce the vanishing gradients problem and achieves strong results on standard computer vision benchmarks<sup>56</sup>. A visualization of PXRDNET’s PXRD Regressor is shown in Figure 11.

## Generative Structure Solution Process

Now, we describe our method for using the CDVAE-inspired model to generate structure solutions, and where we diverge from the original CDVAE formulation. Refer to Figure 12 for an overview.

### Latent Code Selection via PXRD and Formula Guided Backpropagation

PXRDNET modifies CDVAE by incorporating PXRD observations and chemical formulas as conditioning information for the generative process. This is achieved through the property optimization mechanism.

For property optimization to work, at train time, we must first train models to predict the attributes we desire from a material, given its latent code. To this end we the PXRD regressor,  $F_\psi$ , parameterized by a modified DenseNet architecture<sup>56</sup>. This is

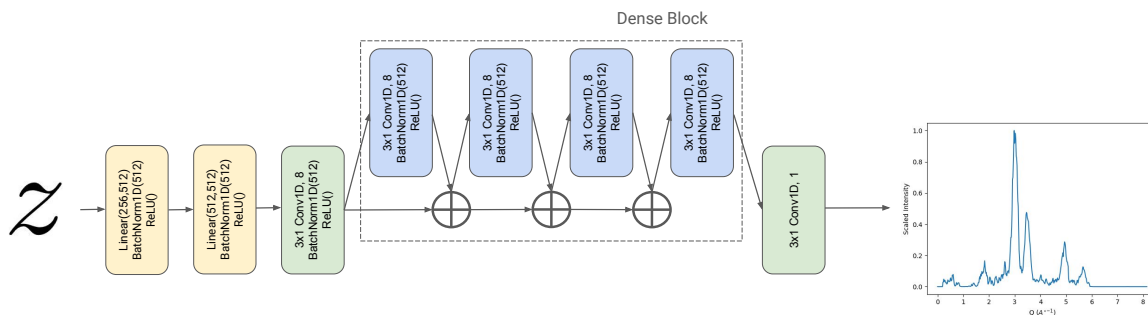


**Figure 11. Visualization of PXRDNET’s PXRD Regressor:** Note  $\oplus$  represents concatenation along the channel dimension.  $F_\psi$  first projects latent material representations  $z \in \mathbb{R}^{256}$  to a 512 dimensional representation via a sequence of fully connected linear layers, 1-dimensional Batch Normalization<sup>57</sup> and ReLU nonlinearity. A single 1-dimensional convolutional layer with a kernel size of 3, followed by a 1-dimensional Batch Normalization, is applied to the projection to produce an 8-channel representation. This representation kicks off the DenseNet feature aggregation, and is passed to a dense block consisting of 4 layers. Each layer maps aggregated features from previous layers in the block to a new 8-channel representation via 1-dimensional convolution with kernel size 3, followed by 1-dimensional Batch Normalization. The dense block produces an 8-channel, 512 dimensional signal. This gets passed through a final 1-dimensional convolutional layer with kernel size 3 to shrink the number of channels to 1 and produce the predicted  $Q$ -space PXRD representation.

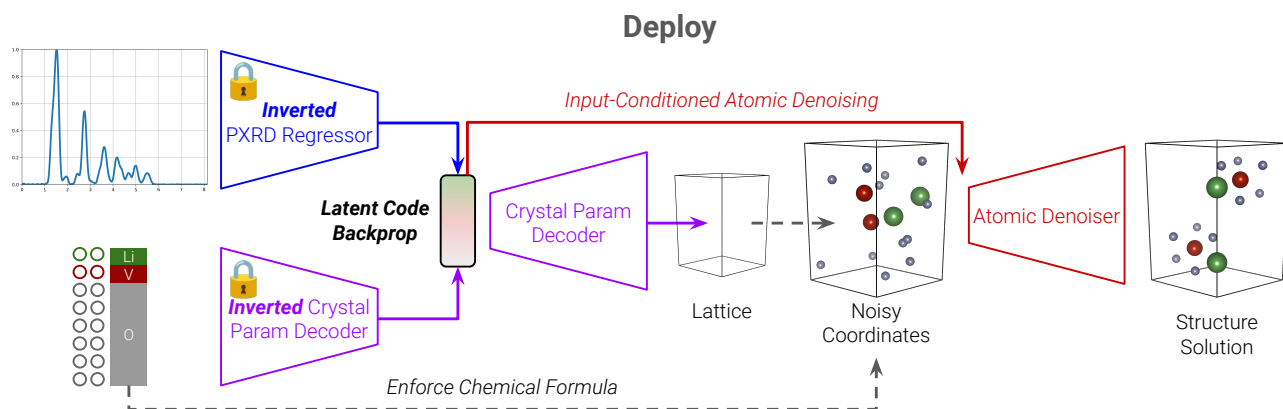


**Figure 12. PXRDNET’s PXRD- and Formula-Guided Structure Solution Process:** PXRDNET’s material generation process uses the same components as the training process (Figure 10), but in a different way. It inverts the PXRD Regressor and Crystal Parameter Decoder; in this way, conditioned on the PXRD and chemical formula, we can generate a latent code that fulfills these properties. We then use the latent code in the same way as the training process, feeding it through the Lattice Decoder and the Atomic Denoiser to generate the structure solution.

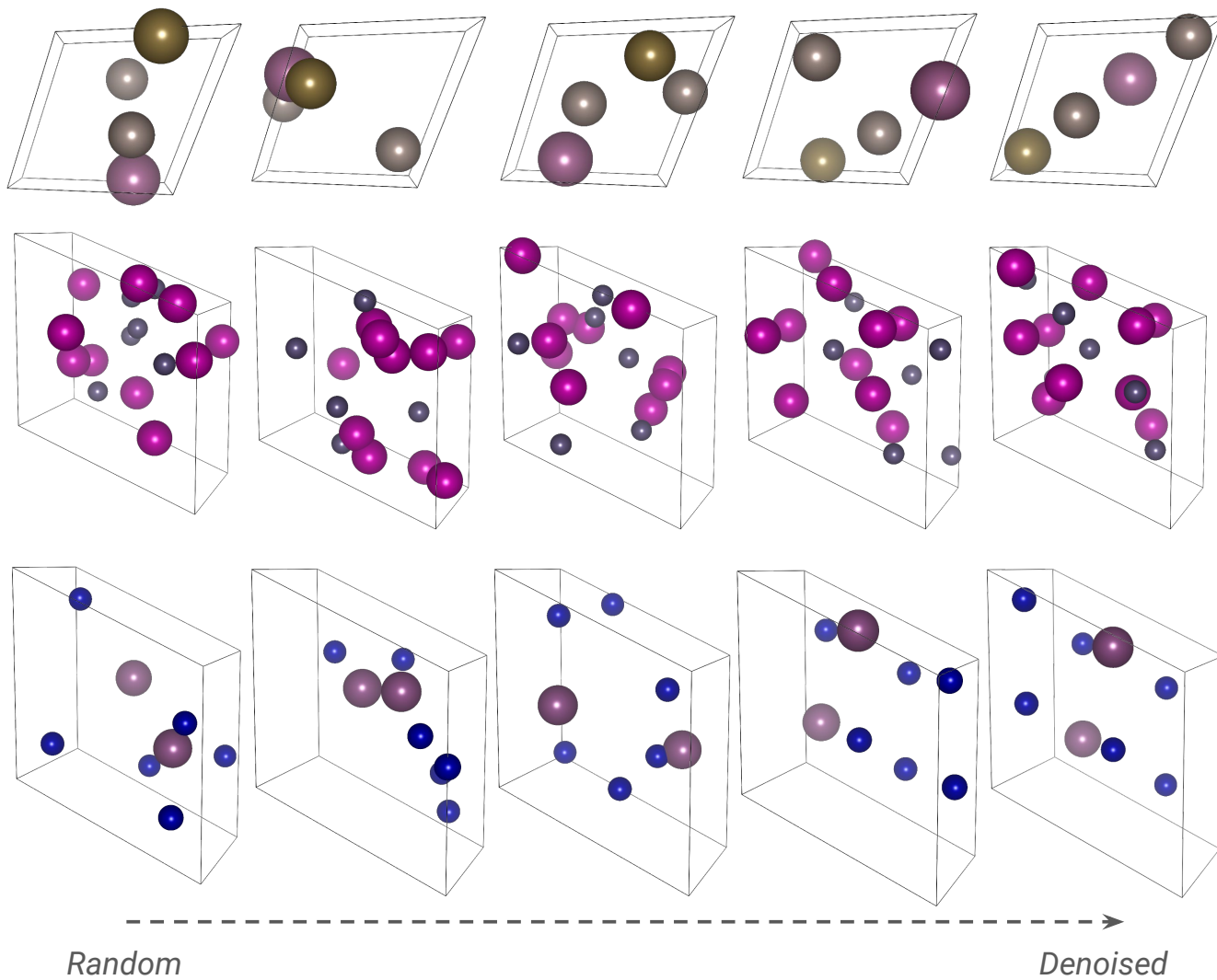


**Figure 13. Visualization of Denoising Diffusion via Langevin Dynamics:** The leftmost column shows randomly initialized atomic coordinates within the unit cell. As we move right, we see the atomic coordinates gradually being denoised into a structural candidate.

jointly trained with the base CDVAE model to predict the observed PXRD pattern of a material from its latent encoding  $z$ . We also train MLPs,  $F_N$  to predict the number of atoms in the unit cell, and  $F_{\text{comp}}$  to predict the chemical composition from  $z$ , as previously described in the variational decoding process.

Then at test time we invert these models such that, conditioned on the attributes of interest (*i.e.*, PXRD pattern, chemical formula), we can get latent codes that adhere to these attributes. Specifically, to generate candidate structure solutions given a PXRD pattern and chemical composition, we apply property optimization to a batch of randomly sampled latent vectors  $z \sim N(0, I)$ . Concretely, we freeze all parameters of PXRDNET and apply gradient descent to adjust each  $z$  to optimize the objective,

$$\min_z \mathcal{L}_{\text{XRD}}(z, y, N, c) = \|F_{\psi}(z) - y\|_1 - \beta \log p(z) + \beta_N \mathcal{L}_{\text{softmax}}(F_N(z), N) + \beta_C \mathcal{L}_{\text{CE}}(F_{\text{comp}}(z), c), \quad (3)$$

where  $y$  is the PXRD pattern of the desired material,  $N$  is the number of atoms in the unit cell,  $c \in \mathbb{R}^{|A|}$  is normalized chemical composition, and  $F_N, F_{\text{comp}}$  are the atom cardinality and composition prediction MLPs. The first two terms in  $\mathcal{L}_{\text{XRD}}$  encourage a latent representation that corresponds to a material with the desired PXRD pattern  $y \in \mathbb{R}^{512}$ , while adhering reasonably to the Gaussian prior on the latent representations  $p(z)$ . The  $\beta$  term controls the degree of adherence to the prior. The last two terms ensure that the latent representation corresponds to a material with the desired number of atoms and chemical composition, and  $\beta_N, \beta_C$  control their respective influences.

We sample and optimize 100 latent vectors  $z$ . We use learning rate ranging from  $0.1 \rightarrow 10^{-4}$  in a cosine decay with warm restarts setting (where each decay period length is doubled upon restart)<sup>58</sup>,  $\beta = 2 * 10^{-4}$ ,  $35000 = 5000 + 10000 + 20000$  total epochs, and  $\beta_N = \beta_C = 0.1$ .

### Candidate Generation with Teacher Forcing

We map the set of optimized latent representations  $z$  (in our setting, we use 100) to materials with the decoding process described previously.  $z$  is used to initialize the lattice, and is used as conditioning for the atomic coordinate denoising process. However, we make a change from the originally described material generation process. We already know the chemical formula. So, we fix the number of atoms and atomic species according to the chemical formula, forgoing the need to use their respective MLPs to predict them again. This technique can be seen as teacher forcing with the strict chemical formula<sup>59,60</sup>, where the strict chemical formula has the absolute quantities of atoms in the unit cell, in addition to the ratios.

Further comparing the training process (Figure 10) to the generative structure solution process (Figure 12), we see that with the exception of the graph encoder, all the same components (atomic denoiser, crystal parameter decoder: composition + atomic cardinality + lattice, PXRD regressor, Gaussian latent code) are used. The difference is that in the structure solution process, the PXRD regressor, the composition decoder MLP, and the atomic cardinality decoder MLP are inverted. In other words, the input is now the PXRD pattern and chemical formula, and the output is a latent code that is optimized via backpropagation while these models are frozen. This results in a latent code that achieves high adherence to the inputted PXRD pattern and chemical formula. Then, the lattice parameter decoder and atomic denoiser are given this latent code (which should contain information about the material structure, based on the PXRD and chemical formula) to generate the lattice parameters and atomic coordinates as before.

### Candidate Filtering via PXRD Simulation

We then simulate the PXRD pattern for each of the 100 candidates with the PyMatGen package<sup>38</sup>. We simulate nanoscale shrinkage and apply Gaussian smoothing on these candidates' simulated PXRD patterns, just as was done for the ground truth PXRD. Finally, the top 5 candidates are selected based on the adherence (measured as  $l_1$  loss) of simulated PXRD to the original, desired PXRD  $y$ . These 5 candidates are treated as PXRDNET's estimate of possible structure solutions of the molecule given the PXRD pattern and chemical composition. (In principle, we can have an arbitrarily high number of candidates, if we wish to expand our search.)

### Training Loop

Unless otherwise specified, we follow the hyperparameter settings in CDVAE<sup>28</sup>. The only major change we make is to adopt a cosine decay with warm restart learning rate schedule, where we have 1000 total epochs, the learning rate ranges from  $5 * 10^{-4} \rightarrow 10^{-6}$ , the initial decay period is 65 epochs, and the number of epochs per decay period is doubled on each restart<sup>58</sup>.

### Baselines

To our knowledge, there exist no *ab initio* end-to-end structure solution methods for nanomaterials (*i.e.*, PXRD pattern and formula as input, structure as output). Thus, to assess the ability of PXRDNET, we conduct two ablations.

### Latent Space Search

For our first ablation, we want to investigate how beneficial our latent code selection process is at creating materials that adhere to the given PXRD and formula information. Thus, we keep all the same parts of our generative structure solution process, except that we do *not* use PXRD or formula information to optimize the latent codes via backpropagation.

Instead, we randomly sample the same number (100) of latent codes from the same distribution  $N(0, I)$  as before. Then, we skip the latent code optimization, and go directly to the decoding process, which is conducted in exactly the same way as our method. That is, we use the same model with the same noise schedule, and we keep the teacher forcing, such that the atomic species and number of atoms are fixed to the true chemical formula. Finally, we do the same candidate filtering with PXRD simulation, to see which of the generated materials matches the ground truth PXRD pattern. Again, we keep the top 5 candidates, and calculate evaluation metrics in exactly the same way as for our method.

### Semi-Random Material Construction

For our next ablation, we want to investigate the importance of the atomic denoising process. So, in addition to removing latent code optimization, we also remove the atomic denoising process.

It is conducted as follows. We randomly sample 100 latent vectors  $z \sim N(0, I)$ , the same number as in the regular material generation process. Without any optimization, we then use these latent vectors (via decoding from our trained MLP) to initialize the unit cells of the materials. As in the other evaluations, we assume that we know the chemical formula, and we randomly initialize the atomic positions, as in our method. The difference is that we do not conduct any denoising on these positions. Then, in exactly the same way as our method, we calculate the PXRD adherence between each of these 100 materials and the ground truth PXRD, and choose the top 5 candidates. From there, evaluation metrics are calculated in the same way as previously described.

This is semi-random, because while  $z$  is randomly drawn from the latent distribution, once it is decoded by the MLP, it does contain priors about physically plausible unit cell shapes. For this reason, this is actually a generous baseline, because it makes use of a small portion of our trained model. Essentially, the only differences between this baseline and our method are (1) the lack of PXRD-guided latent code optimization; (2) the lack of denoising. All other parts are the same, making for a fair comparison.

### Metrics

To quantify PXRDNET performance, we employ a set of rigorously defined metrics to compare candidate and base truth material similarity.

#### Match Rate

First, following prior work<sup>22–25,28,29,38,61,62</sup>, we use `StructureMatcher` from `PyMatGen` with the following default tolerance settings: `stol=0.3`, `angletol=5`, `ltol=0.2`. We note that these tolerance settings are significantly stricter than those used to evaluate the original CDVAE model<sup>28</sup>. We report the rate at which `StructureMatcher` finds a match between the top PXRDNET candidate (as measured by simulated  $I_1$  PXRD difference) and base truth material across 200 materials sampled from the test set. Intuitively, the match rate is the percentage of PXRDNET predicted materials (where the prediction is the best item from the candidate set for a given PXRD pattern) that have approximately the same structure as the true material, within some small error thresholds.

#### PDF Correlation

We also report quantitative results on the similarity between simulated PXRD patterns for PXRDNET candidates and the target PXRD pattern. To quantify PXRD similarity, we convert the candidate and base truth  $Q$ -space PXRD patterns (without any sinc broadening or noise) to their pair-distribution-function counterparts via a sine Fourier transform<sup>3</sup>. Intuitively, pair distribution function measures the distribution of interatomic distances in a material. We then compute the Pearson correlation coefficient (PCC)<sup>37</sup> between the candidate and ground truth PDF patterns. A PCC of 1 indicates the curves are identical and a value of 0 that they curves are completely uncorrelated. PCC can go negative for anti-correlated curves, but this rarely happens in practice when comparing PDFs and so this measure *de facto* varies between 0 and 1 in these tests. This practice follows prior evaluation in the literature<sup>32</sup>. We report the best Pearson correlation value among the 5 PXRDNET candidates.

#### R-Factor

To have a metric that operates directly on the reciprocal space diffraction patterns we also calculate the R-factor (residuals function) defined as,

$$R_{wp}^2 = \frac{\int [I_{\text{gt}}(Q) - I_{\text{pred}}(Q)]^2 dQ}{\int [I_{\text{gt}}(Q)]^2 dQ}, \quad (4)$$

where  $I_{\text{gt}}(Q)$  is the ground truth PXRD pattern in  $Q$ -space, and  $I_{\text{pred}}(Q)$  is the PXRD pattern in  $Q$ -space simulated from the predicted crystalline structure. The PXRD patterns are computed on a grid of 8192 evenly spaced samples in  $Q$  space. Typically,  $R_{\text{wp}}^2$  below 10% can be considered to be a success<sup>3</sup>.

When we calculate this metric, we calculate the PXRD patterns *without* any simulated nanoscale shrinkage. The reason why we omit this is because when comparing the 10 Å experiments to the 100 Å experiments, the different sinc filters would result in different peak broadening widths, and give a non-consistent standard of comparison across these experiments.

Instead, we consistently apply a Gaussian filtering on the PXRD patterns with  $\sigma = 0.040784 \text{ \AA}^{-1}$  (this is only 0.5% of the PXRD pattern width). The rationale for this is that if we were to use the raw PXRD patterns without any peak broadening, a negligible difference in peak location (let us say,  $10^{-6} \text{ \AA}$ ) would actually lead to a very poor  $R_{\text{wp}}^2$ , since the integral in the numerator calculates the error at each infinitesimally small location. However, it should be clear that such an example is indeed a good fit. So, to avoid this problem, we add the slight Gaussian peak broadening, such that if the peaks are "close enough", we will still have low error values. We note that varying the width of this Gaussian will change the resulting agreement factors, and so the absolute value of this measure does not carry definitive information, but the relative value between solutions certainly does.

Finally, just as with the PDF correlation, we report the best  $R_{\text{wp}}^2$  among the 5 PXRDNET candidates for each material.

## Structural Refinement Pipeline

As described in the text we carry out a Rietveld refinement on the results of a small subset of materials as would be done in a conventional structure solution procedure.

### Material Curation

Our intention was to randomly sample 20 materials for Rietveld refinement, which we did by uniformly selecting materials from the test set. For each of these materials, we picked a high-performing one of the top-5 candidates, which was then Rietveld refined.

### PXRD Pre-Processing

We used the PXRD patterns from both the simulated 10 Å and 100 Å nanomaterial sizes. We convolved the 10 Å patterns with a Gaussian filter with low sigma ( $0.081568 \text{ \AA}^{-1} = 1\%$  of pattern length in  $Q$ ), and we convolved the 100 Å patterns with a lower-sigma filter ( $0.040784 \text{ \AA}^{-1} = 0.5\%$  of pattern length in  $Q$ ).

### Rietveld Refinement Parameters

Since the lattice parameters and space group symmetry (all in  $PI$ ) of the predictions are different than the ground truth, the simulated diffraction patterns of the predictions are typically different than those of the ground truth despite the topological similarity. We performed a constrained search over distortions of the predicted unit cell via refinements using the program TOPAS v7<sup>63</sup>. Due to the different simulation engine, we first ensured a suitable profile to describe the peak-shape by fitting the ground truth model to the ground truth simulated data using a Gaussian convolution for the 100 Å and the 10 Å patterns. The resulting values were then fixed for refinements of PXRDNET candidates, which had been simulated with the same Gaussian filter as the ground-truth patterns. For each predicted structure, all lattice parameters were then allowed to refine within a window of  $\pm 20\%$  along with a scale factor, where the parameters were randomized after each convergence to escape local minima over 2000 iterations. Due to the low model symmetry and low angular range and high broadening of the patterns, we did not attempt to additionally refine the atom site positions. This is in contrast to the final refinement step in conventional structure solution from crystalline materials and so we do not expect to obtain  $R_{\text{wp}}$  values as good as those from full refinements, even for correct structures.

### R-Factor Comparison

Finally, we compare the pre-refinement  $R_{\text{wp}}^2$  to the post-refinement  $R_{\text{wp}}^2$ . A goal here is to look for correlations between metrics for structures that are successful pre and post refinement. If there is a strong correlation we can use pre-refinement metrics as a low cost proxy for models that will perform well post-refinement.

Although during the Rietveld refinement, we optimize  $R_{\text{wp}}^2$  from the material degraded by concurrent sinc and Gaussian convolutions, for this comparison, we compare all the  $R_{\text{wp}}^2$  (both pre- and post- refinement) *without* any simulated nanoscale broadening but with the low-sigma Gaussian broadening only. We feel that this gives a better assessment of the true quality of the structure solution. See "Metrics/R-Factor" for more details on the calculations.

## References

1. Giacovazzo, C. *Fundamentals of crystallography*, vol. 7 (Oxford university press, USA, 2002).

2. Billinge, S. J. & Levin, I. The problem with determining atomic structure at the nanoscale. *science* **316**, 561–565 (2007).
3. Dinnebier, R. E. & Billinge, S. J. *Powder diffraction: theory and practice* (Royal society of chemistry, 2008).
4. Egami, T. & Billinge, S. J. *Underneath the Bragg peaks: structural analysis of complex materials* (Newnes, 2012).
5. Juhás, P., Cherba, D., Duxbury, P., Punch, W. & Billinge, S. Ab initio determination of solid-state nanostructure. *Nature* **440**, 655–658 (2006).
6. Juhas, P., Granlund, L., Gujarathi, S. R., Duxbury, P. M. & Billinge, S. J. Crystal structure solution from experimentally determined atomic pair distribution functions. *J. Appl. Crystallogr.* **43**, 623–629 (2010).
7. Billinge, S. J. & Proffen, T. Machine learning in crystallography and structural science (2024).
8. Choudhary, K. *et al.* Recent advances and applications of deep learning methods in materials science. *npj Comput. Mater.* **8**, 59 (2022).
9. Oviedo, F. *et al.* Fast and interpretable classification of small x-ray diffraction datasets using data augmentation and deep neural networks. *npj Comput. Mater.* **5**, 60 (2019).
10. Suzuki, Y. *et al.* Symmetry prediction and knowledge discovery from x-ray diffraction patterns using an interpretable machine learning approach. *Sci. reports* **10**, 21790 (2020).
11. Park, W. B. *et al.* Classification of crystal structure using a convolutional neural network. *IUCrJ* **4**, 486–494 (2017).
12. Lee, J.-W., Park, W. B., Lee, J. H., Singh, S. P. & Sohn, K.-S. A deep-learning technique for phase identification in multiphase inorganic compounds using synthetic xrd powder patterns. *Nat. communications* **11**, 86 (2020).
13. Aguiar, J., Gong, M. L., Unocic, R., Tasdizen, T. & Miller, B. Decoding crystallography from high-resolution electron imaging and diffraction datasets with deep learning. *Sci. Adv.* **5**, eaaw1949 (2019).
14. Ziletti, A., Kumar, D., Scheffler, M. & Ghiringhelli, L. M. Insightful classification of crystal structures using deep learning. *Nat. communications* **9**, 2775 (2018).
15. Tiong, L. C. O., Kim, J., Han, S. S. & Kim, D. Identification of crystal symmetry from noisy diffraction patterns by a shape analysis and deep learning. *npj Comput. Mater.* **6**, 196 (2020).
16. Garcia-Cardona, C. *et al.* Learning to predict material structure from neutron scattering data. In *2019 IEEE International Conference on Big Data (Big Data)*, 4490–4497 (IEEE, 2019).
17. Merker, H. A. *et al.* Machine learning magnetism classifiers from atomic coordinates. *Iscience* **25** (2022).
18. Maffettone, P. M. *et al.* Crystallography companion agent for high-throughput materials discovery. *Nat. Comput. Sci.* **1**, 290–297 (2021).
19. Szymanski, N. J., Bartel, C. J., Zeng, Y., Tu, Q. & Ceder, G. Probabilistic deep learning approach to automate the interpretation of multi-phase diffraction spectra. *Chem. Mater.* **33**, 4204–4215 (2021).
20. Uryu, H. *et al.* Deep learning enables rapid identification of a new quasicrystal from multiphase powder diffraction patterns. *Adv. Sci.* **11**, 2304546 (2024).
21. Szymanski, N. J. *et al.* An autonomous laboratory for the accelerated synthesis of novel materials. *Nature* **624**, 86–91 (2023).
22. Jiao, R. *et al.* Crystal structure prediction by joint equivariant diffusion. *Adv. Neural Inf. Process. Syst.* **36** (2024).
23. Pakornchote, T. *et al.* Diffusion probabilistic models enhance variational autoencoder for crystal structure generative modeling. *Sci. Reports* **14**, 1275 (2024).
24. Antunes, L. M., Butler, K. T. & Grau-Crespo, R. Crystal structure generation with autoregressive large language modeling. *arXiv preprint arXiv:2307.04340* (2023).
25. Zhao, Y. *et al.* Physics guided deep learning for generative design of crystal materials with symmetry constraints. *npj Comput. Mater.* **9**, 38 (2023).
26. Merchant, A. *et al.* Scaling deep learning for materials discovery. *Nature* **624**, 80–85 (2023).
27. Yang, M. *et al.* Scalable diffusion for materials generation. *arXiv preprint arXiv:2311.09235* (2023).
28. Xie, T., Fu, X., Ganea, O.-E., Barzilay, R. & Jaakkola, T. Crystal diffusion variational autoencoder for periodic material generation. *arXiv preprint arXiv:2110.06197* (2021).
29. Zeni, C. *et al.* Mattergen: a generative model for inorganic materials design. *arXiv preprint arXiv:2312.03687* (2023).

30. Guo, G. *et al.* Towards end-to-end structure solutions from information-compromised diffraction data via generative deep learning. *arXiv preprint arXiv:2312.15136* (2023).
31. Kjær, E. T. *et al.* DeepStruc: Towards structure solution from pair distribution function data using deep generative models. *Digit. Discov.* **2**, 69–80 (2023).
32. Kjær, E. *et al.* MlstructureMining: A machine learning tool for structure identification from x-ray pair distribution functions. *Digit. Discov.* (2024).
33. Dun, C. *et al.* CrysFormer: Protein structure prediction via 3d patterson maps and partial structure attention. *arXiv preprint arXiv:2310.03899* (2023).
34. Pan, T., Jin, S., Miller, M. D., Kyrillidis, A. & Phillips, G. N. A deep learning solution for crystallographic structure determination. *IUCrJ* **10**, 487–496 (2023).
35. Song, Y. & Ermon, S. Generative modeling by estimating gradients of the data distribution. *Adv. neural information processing systems* **32** (2019).
36. Jain, A. *et al.* Commentary: The materials project: A materials genome approach to accelerating materials innovation. *APL materials* **1** (2013).
37. Lee Rodgers, J. & Nicewander, W. A. Thirteen ways to look at the correlation coefficient. *The Am. Stat.* **42**, 59–66 (1988).
38. Ong, S. P. *et al.* Python materials genomics (pymatgen): A robust, open-source python library for materials analysis. *Comput. Mater. Sci.* **68**, 314–319 (2013).
39. Kreyling, W. G., Semmler-Behnke, M. & Chaudhry, Q. A complementary definition of nanomaterial. *Nano today* **5**, 165–168 (2010).
40. Lathi, B. P. & Green, R. A. *Linear systems and signals*, vol. 2 (Oxford University Press New York, 2005).
41. Cheetham, A. K. & Seshadri, R. Artificial intelligence driving materials discovery? perspective on the article: Scaling deep learning for materials discovery. *Chem. Mater.* **36**, 3490–3495 (2024).
42. Leeman, J. *et al.* Challenges in high-throughput inorganic materials prediction and autonomous synthesis. *PRX Energy* **3**, 011002 (2024).
43. Szymanski, N. J. *et al.* Toward autonomous design and synthesis of novel inorganic materials. *Mater. Horizons* **8**, 2169–2198 (2021).
44. David, W. I., Shankland, K., McCusker, L. B. & Baerlocher, C. *Structure determination from powder diffraction data*, vol. 13 (OUP Oxford, 2006).
45. Checkcif. <https://checkcif.iucr.org/>. Accessed 06/15/24.
46. <https://www.iucr.org/resources/data/databases>.
47. Juhás, P., Granlund, L., Duxbury, P., Punch, W. & Billinge, S. The liga algorithm for ab initio determination of nanostructure. *Acta Crystallogr. Sect. A: Foundations Crystallogr.* **64**, 631–640 (2008).
48. Toby, B. 4.2. powder dictionary (pdCIF). *Int. Tables for Crystallogr. Vol. G: Defin. exchange crystallographic data* 258–269 (2006).
49. Shannon, C. Communication in the presence of noise. *Proc. IRE* **37**, 10–21, DOI: [10.1109/JRPROC.1949.232969](https://doi.org/10.1109/JRPROC.1949.232969) (1949).
50. Kingma, D. P. & Welling, M. Auto-encoding variational bayes (2022). [1312.6114](https://arxiv.org/abs/1312.6114).
51. Yang, L. *et al.* Diffusion models: A comprehensive survey of methods and applications. *ACM Comput. Surv.* **56**, 1–39 (2023).
52. Gasteiger, J., Groß, J. & Günnemann, S. Directional message passing for molecular graphs. *arXiv preprint arXiv:2003.03123* (2020).
53. Xie, T. & Grossman, J. C. Crystal graph convolutional neural networks for an accurate and interpretable prediction of material properties. *Phys. review letters* **120**, 145301 (2018).
54. Song, Y. & Ermon, S. Generative modeling by estimating gradients of the data distribution (2020). [1907.05600](https://arxiv.org/abs/1907.05600).
55. Gasteiger, J., Becker, F. & Günnemann, S. Gemnet: Universal directional graph neural networks for molecules. *Adv. Neural Inf. Process. Syst.* **34**, 6790–6802 (2021).
56. Huang, G., Liu, Z., van der Maaten, L. & Weinberger, K. Q. Densely connected convolutional networks (2018). [1608.06993](https://arxiv.org/abs/1608.06993).



57. Ioffe, S. & Szegedy, C. Batch normalization: Accelerating deep network training by reducing internal covariate shift (2015). [1502.03167](https://arxiv.org/abs/1502.03167).
58. Loshchilov, I. & Hutter, F. Sgdr: Stochastic gradient descent with warm restarts. *arXiv preprint arXiv:1608.03983* (2016).
59. Goodfellow, I., Bengio, Y. & Courville, A. *Deep learning* (MIT press, 2016).
60. Williams, R. J. & Zipser, D. A learning algorithm for continually running fully recurrent neural networks. *Neural computation* **1**, 270–280 (1989).
61. Hicks, D. *et al.* Aflow-xtalfinder: a reliable choice to identify crystalline prototypes. *npj Comput. Mater.* **7**, 30 (2021).
62. Thomas, J. C., Natarajan, A. R. & Van der Ven, A. Comparing crystal structures with symmetry and geometry. *npj Comput. Mater.* **7**, 164 (2021).
63. Coelho, A. A. Topas and topas-academic: an optimization program integrating computer algebra and crystallographic objects written in c++. *J. Appl. Crystallogr.* **51**, 210–218 (2018).

## Acknowledgements

We thank Judah Goldfeder for helpful discussions regarding the viability of a diffusion-based approach. We thank Ethan Bondick and Hao Lin for their assistance in preliminary materials visualization.

## Author contributions statement

SJLB and HL proposed the research topic. GG and TLS proposed the machine learning methodology and wrote the code. GG, TLS, and SJLB conducted the theoretical nanomaterial shrinkage analysis. GG and SJLB procured the data. GG, SJLB, and HL designed the experiments. MWT conducted structural refinement. All authors wrote the manuscript and provided feedback.

## Additional information

Work in the Lipson group was supported by U.S. National Science Foundation under AI Institute for Dynamical Systems grant 2112085. Work in the Billinge group was supported by the U.S. Department of Energy, Office of Science, Office of Basic Energy Sciences (DOE-BES) under contract No. DE-SC0024141.

## Code Availability

Please obtain the code, with reproducibility instructions, at: [https://github.com/gabeguo/cdvae\\_xrd](https://github.com/gabeguo/cdvae_xrd).

## Data Availability

MP-20-PXRD is available at: [https://github.com/gabeguo/cdvae\\_xrd/tree/main/data/mp\\_20](https://github.com/gabeguo/cdvae_xrd/tree/main/data/mp_20). Instructions for obtaining the experimental data are available at: [https://github.com/gabeguo/cdvae\\_xrd/tree/main/data/experimental\\_xrd](https://github.com/gabeguo/cdvae_xrd/tree/main/data/experimental_xrd).